

# We are IntechOpen, the world's leading publisher of Open Access books Built by scientists, for scientists

6,900

Open access books available

186,000

International authors and editors

200M

Downloads

Our authors are among the

154

Countries delivered to

TOP 1%

most cited scientists

12.2%

Contributors from top 500 universities



WEB OF SCIENCE™

Selection of our books indexed in the Book Citation Index  
in Web of Science™ Core Collection (BKCI)

Interested in publishing with us?  
Contact [book.department@intechopen.com](mailto:book.department@intechopen.com)

Numbers displayed above are based on latest data collected.  
For more information visit [www.intechopen.com](http://www.intechopen.com)



# Microstructural Evolution During the Homogenization of Al-Zn-Mg Aluminum Alloys

Ali Reza Eivani<sup>1,2</sup>, Jie Zhou<sup>2</sup> and Jurek Duszczek<sup>2</sup>

<sup>1</sup>*Materials Innovation Institute (M2i), Mekelweg 2, 2628 CD Delft,*

<sup>2</sup>*Department of Materials Science and Engineering, Delft University of Technology, Mekelweg 2, 2628 CD Delft, The Netherlands*

## 1. Introduction

### 1.1 Background

Aluminum and aluminum alloys are probably the most ideal materials for extrusion, and they are the most commonly extruded. Most of commercially available aluminum alloys can be extruded. Principal applications include parts for the aircraft and aerospace industries, pipes, wires, rods, bars, tubes, hollow shapes, cable sheathing, for the building, automotive and electrical industries. Sections can be extruded from heat-treatable or non-heat treatable low-, medium- and high-strength aluminum alloys [1].

In the last 30 years, the development of aluminum extrusion technology has, in the main, been focused on the billet metallurgy, die design and process control for low- and medium-strength aluminum alloys in the 6xxx series for architectural applications, in order to maximize extrusion speed and at the same time fulfill the requirements in product specifications in terms of dimensions, shape, surface and mechanical properties. As a result, there is a wealth of information available on the relationship between alloy chemistry, microstructure and extrudability of these alloys [2]. In comparison, the fundamental knowledge and extrusion technology, especially those for medium- and high-strength aluminum alloys in 7xxx series, are rather scarce in the open literature [2].

7xxx series aluminum alloys, almost exclusively for air transport applications in the past but now increasingly used in the rail and road vehicles, must comply with much more stringent performance specifications than 6xxx series aluminum alloys for architectural applications. Although many investigations on the behavior of medium- and high-strength aluminum alloys at individual processing steps have been performed, systematic research linking all these processing steps is lacking, while the extrusion behavior is associated with alloy composition and a series of microstructural evolutions throughout the whole chain of material processing from casting through homogenization to extrusion. Such research is particularly needed for the aluminum extrusion companies that are currently shifting the application fields of extrusions from architecture to ground transport where medium-strength alloys (7003, 7005, 7010, 7020, 2011, 2017 and 2618) and high-strength alloys (7049, 7050, 7075 and 2024) are increasingly used. This chapter concerns one of the mostly used medium-strength alloys, AA7020, as a representative of Cu-free 7xxx series aluminum alloys. Table 1 shows the nominal chemical composition of the AA7020 aluminum alloy.

Element	Si	Fe	Cu	Mn	Mg	Zn	Ti	Cr	Zr	Al
Wt. %	<0.35	<0.35	<0.2	0.05 – 0.5	1.0 – 1.4	4.0 - 5.0	Zr + Ti = 0.08-0.25	0.1 – 0.4	0.08 – 0.20	Bal.

Table 1. Nominal chemical composition of the AA7020 aluminum alloy

It should be noted that despite a broad range of applications, the AA7xxx series alloys have a number of characteristics that are not favorable for material processing, for example, low extrudability, high extrusion pressure required together with low solidus temperature which can cause incipient melting, makes their production at low throughputs. In addition, in the 7xxx series aluminum alloys including the AA7020 alloy, due to the long solidification interval (the temperature gap between the liquidus and solidus), microsegregation tends to be significant and homogenization needs lots of time, which causes the formation of second phase particles, some of which may be detrimental to the hot workability of the alloy as well as its final mechanical properties. Furthermore, the formation of a peripheral coarse grain structure is quite common in these alloys which can significantly degrade the mechanical properties. These issues will be discussed as limiting factors in the extrusion of the AA7020 aluminum alloy.

1.2 Limiting factors in the extrusion of AA7020

Numerous limiting factors, e.g., the formation of defects, low extrudability and the complications in the final microstructure of the product in 7xxx series aluminum alloys can impair the productivity of the extrusion process [2]. Most of the limiting factors are directly or indirectly related to the chemical composition, metallurgical features formed DC casting and evolving during the homogenization treatment, and extrusion conditions [2]. Using an optimum chemical composition within the allowance range of a specific alloy, in combination with optimum homogenization and extrusion conditions can result in a significant increase of the extrudability of the material and improvement of the mechanical properties of the final product. This requires the knowledge of the factors presented below, i.e., hot workability and peripheral recrystallization, both of which are strongly dependent on chemical composition of the alloy and the homogenization treatment.

1.2.1 Hot workability

For wrought aluminum alloys, hot workability is an important index of manufacturability. It refers to the capacity of an alloy to withstand hot deformation at a maximum rate without inducing flow non-uniformity or structural defects. If translated into extrusion (termed extrudability), it is defined as the maximum speed for a sound extrudate with sufficient dimension and shape accuracy. Hot workability is in fact affected by all parameters affecting the fracture of the material under processing [1]. It is strongly dependent on the size and density of second-phase particles which are in turn dependent on the chemical composition and homogenization treatment. On the other hand, compressive stresses superimposed on shear stresses during the deformation process can have a significant influence on closing small cavities or limiting their growth and thus enhancing workability. Because of the important role of the stress state, it is not possible to express workability in absolute terms. Workability depends not only on material characteristics but also on process variables, such as strain, strain rate, temperature, and stress state [1]. In other words, extrudability can be deteriorated by two factors: (i) unfavorable processing conditions and (ii) the presence of large second-phase particles.

Investigation of the effect of processing conditions on the hot workability of AA7xxx series aluminum alloys is out of the scope of this chapter. However, the effect of particles which would deteriorate the hot workability of the alloy is the main subject of this chapter.

High-strength aluminum alloys (7xxx series) are known for having rather poor hot workability due to the presence of dissolved and later precipitated elements in the form of large particles that raise flow stress and cause the actual temperature of the extrudate to increase above the solidus temperature, leading to hot tearing as shown in Fig. 1. Hot tearing represents the separation or failure of the product as a result of a sequence of phenomena consisting of local melting, crack formation and final fracture of the product. Hot tearing may occur as a result of the presence of large intermetallic particles or even the multiplication of the two mentioned factors (local melting and large particles). Therefore, in hot extrusion, applicable extrusion speed depends on the alloy composition and the microstructure formed during direct-chill casting and developed during homogenization, cooling and reheating to the initial billet temperature.



Fig. 1. Extreme case of hot tearing in AA7075 aluminum alloy [3]

In the case of the 7xxx series alloys, the two phases that deteriorate the extrudability are (i) compounds of Al-Fe-Mn-Si elements, which are especially important if they are located at the grain boundaries and (ii) Al-Mg-Zn-Cu eutectic phases which are mostly located at the dendrite boundaries.

#### 1.2.1.1 Particles composed of Al, Fe, Mn and Si

It has been proven that in the case of the AA7020 aluminum alloy Al, Fe, Mn and Si-containing particles have the  $\text{Al}_{17}(\text{Fe}_{3.2}\text{Mn}_{0.8})\text{Si}_2$  stoichiometric composition and are mostly located at the grain boundaries and therefore are called GB particles [4]. GB particles deteriorate the hot workability of the alloy in addition to mechanical properties since they are hard and brittle especially when located at the grain boundary regions. In order to avoid the detrimental effects of these particles, they should be dissolved during the homogenization treatment. If the particles are not dissolvable, they should be spheroidized.

#### 1.2.1.2 Particles composed of Al, Mg, Zn and Cu

During the solidification of the 7xxx series aluminum alloys containing Mg, Zn and Cu, some intermetallic particles such as  $\text{Al}_6\text{CuMg}_4$ ,  $\text{Al}_2\text{Mg}_3\text{Zn}_3$ ,  $\text{AlCuMg}$ ,  $\text{MgZn}_2$ ,  $\text{Al}_2\text{Cu}$  and  $\text{MgZn}_2$  phases form [5-9]. In addition, mutual solutions of different phases can result in the formation of new particles, for example, mutual solid solution of  $\text{Al}_6\text{CuMg}_4$  and  $\text{Al}_2\text{Mg}_3\text{Zn}_3$  compounds (T phase), solid solution between  $\text{AlCuMg}$  and  $\text{MgZn}_2$  compounds (M phase), solid solution formed by  $\text{Al}_5\text{Cu}_6\text{Mg}_2$  and  $\text{Mg}_2\text{Zn}$  compounds (Z phase) and between  $\text{Al}_2\text{CuMg}$  and  $\text{Al}_2\text{Cu}$  compounds (S phase). The investigation of these particles is interesting for hot working since they mostly have low melting points, which may result in incipient melting during hot deformation.



1.2.2 Peripheral recrystallization

In addition to high flow stress and low solidus temperature, local recrystallization is another factor limiting the extrusion window of medium- and high-strength aluminum alloys. For ground and air transport applications, a qualified extrudate should not contain any undesirable microstructural features, most notably local recrystallized, excessively large grains.

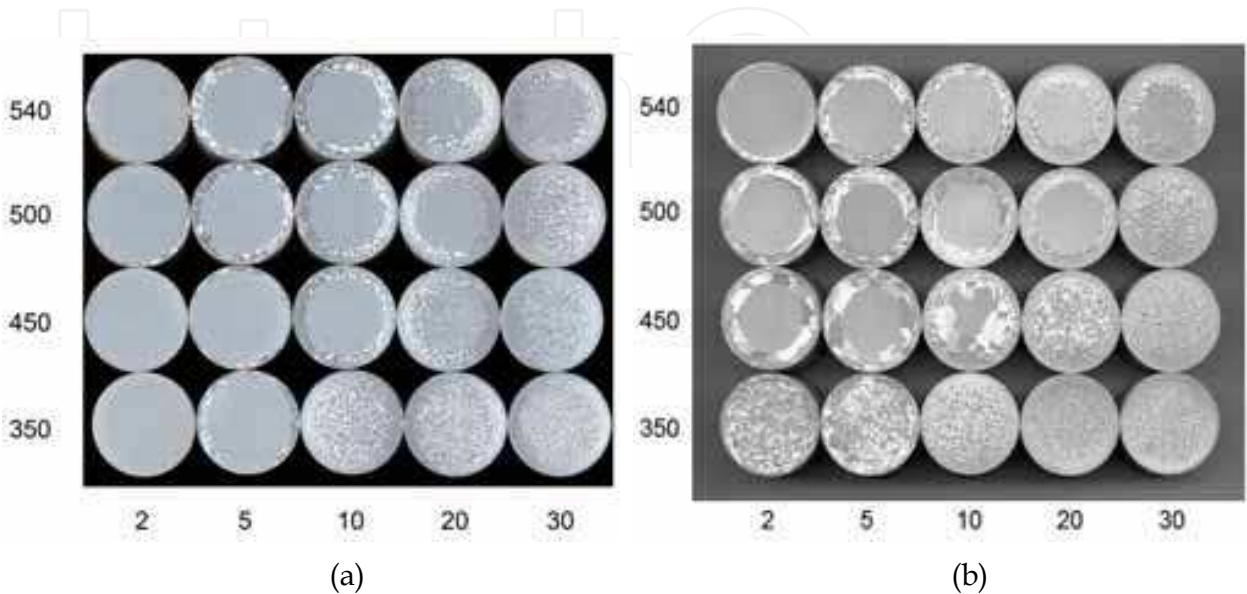


Fig. 2. Macrostructures of AA6005 25 mm bar varying with ram speed (mm/s) and billet temperature (a) as extruded and (b) after solution heat treatment [10, 11]

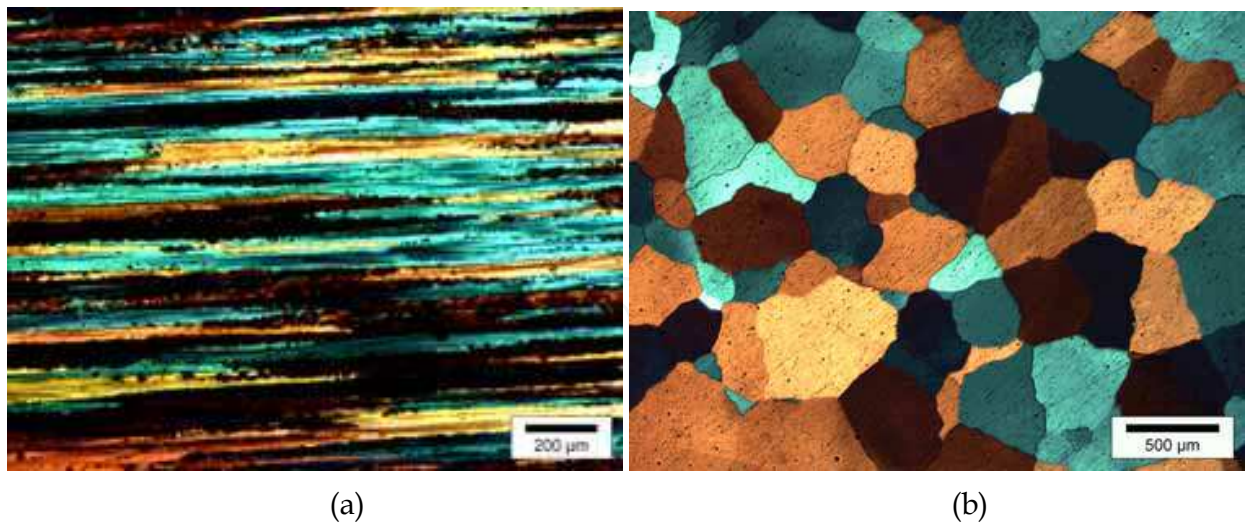


Fig. 3. Grain structures of (a) the core and (b) periphery of AA7020 extruded at 450 °C, 3 m/min and 15:1 [12]

The microstructure of an extruded aluminum product varies from an unrecrystallized fibrous structure to a thoroughly recrystallized fine or coarse grain structure (Fig. 2), depending on the chemical composition, homogenization treatment and extrusion conditions, i.e., speed and temperature, and cooling procedure [10, 11]. The most undesirable

microstructure is the one with a peripheral coarse grain (PCG) structure [2] which is a well known defect in hot extruded aluminum alloys. In this case, the peripheral surfaces of the structure are fully recrystallized, having large grains, while the core is composed of unrecrystallized elongated grains as shown in Fig. 3.

PCG degrades the properties of the extruded product such as strength, fracture toughness and stress corrosion resistance [2]. It is actually a perpetual problem that extruders encounter in meeting the specifications of aircraft alloys that base their strength requirements on typical longitudinal properties of the unrecrystallized core and assume implicitly that no recrystallized outer band structure is present. It is generally understood that the peripheral recrystallization is a complex interplay of billet composition (grain growth inhibitors, i.e., Mn, Cr, or Zr), microstructure, deformation conditions and critical temperatures (solvus, solidus and recrystallization) [2, 3, 10-12].

### 1.3 Application of homogenization treatment

A homogenization treatment after DC casting for the 7xxx alloys is meant to serve the purposes of dissolving second-phase particles and generating dispersoids that are able to inhibit recrystallization and PCG zone formation. The metallurgical features that occur during DC casting and should be studied during the homogenization treatment are presented below.

1. The mechanical properties of extruded products are largely dependent on alloying elements present in solid solution. These elements increase the strength mainly through solid solution or precipitation hardening [13]. During casting of aluminum alloys, a large fraction of alloying elements segregate to the liquid and result in an inhomogeneous distribution of alloying elements. Therefore, removal of the inhomogeneous distribution of alloying elements on a microscale is of prime importance during the homogenization treatment.
2. Segregation can also result in the formation of eutectic constitutive particles with low melting points in the grain boundary regions or inside the grains [14, 15]. As mentioned earlier, the presence of low melting point (LMP) phases which may cause incipient melting during hot deformation can deteriorate the hot workability of aluminum alloys. Therefore, one of the aims of the homogenization treatment is to dissolve LMP phases.
3. In addition, the formation of some hard particles with sharp edges mostly from impurities, e.g., Fe, in combination with some alloying elements such as Mn and Si is expected during DC casting. These particles also decrease the hot workability and limit the range of process parameters applicable during extrusion [2, 14, 16-19]. Therefore, it is necessary to dissolve these particles as well, in order to obtain high mechanical properties and extrudability. If the dissolution of these particles is exhibitively energy and time consuming, these particles should be spheroidized.
4. Eliminating the PCG structure or decreasing its extent is of great interest to the aluminum extrusion industry. It is generally known that the formation of small dispersoid particles can pin the low and high angle grain boundaries and therefore, inhibit recrystallization and grain growth. Therefore, an optimum homogenization treatment should take the formation of fine, well-distributed dispersoid particles into account.

### 1.4 Previous works on homogenization treatment of aluminum alloys

Although there have been a number of investigations on the homogenization treatment of the 7xxx series aluminum alloys in recent years [5-8, 20-26], most of the efforts have been

focused on the nature and evolution of the  $\text{Al}_2\text{Mg}_3\text{Zn}_3$  (T),  $\text{Al}_2\text{CuMg}$  (S),  $(\text{CuZnAl})_2\text{Mg}$  and  $\text{MgZn}_2$  ( $\eta$ ) phases [5-9] and the formation and distribution of dispersoids during homogenization [20-26]. In addition, in comparison with other aluminum alloys, the information on the 7xxx series aluminum alloys is rather scarce in the literature. Although some researchers have studied the microstructural changes and the evolution of the eutectic and low melting point phases during homogenization in the case of the 7xxx series aluminum alloys, there is still a lack of information in the case of the AA7020 aluminum alloy. Moreover, there has been no comprehensive quantitative study on the dependence of the particles on homogenization treatment parameters. Most of the investigations are concerned with the microstructural evolution and phase transformations during homogenization, describing the phenomena in a qualitative manner. For example, Lim et. al. [6] investigated the effects of compositional changes and preheating conditions on the evolution of constitutive particles, the M, T, S phases and dispersoids in AA7175 and AA7050 alloys. Senkov et. al. [27] studied the effect of homogenization treatment on the microstructural evolution of four newly developed 7xxx series aluminum alloys to obtain optimized conditions. Jackson and Sheppard [14] studied the effect of homogenization treatment on the microstructural changes of AA7075, 7150 and 7049 alloys. They focused on the evolution of the microstructure, low melting point phases and the M, T, S,  $\text{Al}_3\text{Mg}_2$  ( $\beta$ ),  $\beta$ ,  $\text{Al}_{18}\text{Cr}_2\text{Mg}$  (E) and  $\text{CrAl}_7$  phases. Fan et al. [28] studied the evolution of microstructure in an Al-Zn-Mg-Cu alloy during homogenization. Ciach et. al. [29] conducted theoretical and experimental studies on the dendritic structure and its dissolution in aluminum-zinc alloys. However, the research on the commercially important AA7020 alloy is scarce. No quantitative investigation on the microstructural evolution in AA7020 regarding the grain boundary particles and low melting point phases during homogenization has been carried out.

As mentioned earlier, in addition to the dissolution of particles, dispersoid formation is another important aim of the homogenization treatment. Dispersoids exert a retarding force or pressure on low angle and high angle grain boundaries, which has a profound effect on the behavior of aluminum alloys in terms of recovery, recrystallization and grain growth [30]. A large amount of experimental research in addition to modeling efforts [15, 20, 24-26, 31-42] has been carried out to understand the conditions under which the dispersoids form and the effect of homogenization parameters on the evolution of dispersoids, with the aim of maximizing the effect of pinning the grain boundaries to retard recrystallization and grain growth. Most of the previous research [15, 20, 25, 42] focused on  $\text{Al}_3\text{Zr}$  as the only dispersoids present in the microstructures of the AA7xxx series aluminum alloys. However, the formation of the other types of dispersoids in other series of aluminum alloys has been a subject of extensive research. For example, in the AA3xxx series aluminum alloys, the formation of Mn-containing dispersoids and their effect on the recrystallization behavior were investigated [31-33]. In the AA6xxx series aluminum alloys, different kinds of dispersoids, i.e., Zr-, Mn- and Cr-containing ones were found to play individual roles in recrystallization inhibition [34-38]. In the case of the AA7xxx series aluminum alloys, the formation of Zr- and Sc-containing dispersoids has been investigated [15, 20, 25, 42]. For example, Robson et al. [15, 20, 25, 42], investigated the effect of Zr addition on the dispersoid formation and recrystallization fraction after hot deformation. It was concluded that using an optimum two-step homogenization treatment, a smaller fraction of recrystallization could be obtained. Robson [25] further studied the effect of Sc on the formation of dispersoids, as Sc was expected to eliminate the dispersoid free zones, as observed in the scandium free AA7050 alloy, thus greatly increasing the recrystallization resistance.

Comprehensive investigations to characterize Cr- and Mn-containing dispersoids formed in the AA7xxx series aluminum alloys during homogenization are scarce, although Cr-, Zr-, and Mn-containing dispersoids commonly co-exist in these alloys. Since analyzing all the individual dispersoids during the investigations to optimize the homogenization treatments is practically impossible, clear characterization of different types of dispersoids with a combination of analytical methods is of prime importance.

The objectives of this research were to determine the effect of homogenization treatment on the evolution of the particles, especially the grain boundary and low melting point ones, and to establish the correlations of the process parameters such as time and temperature with the fractions of these particles in the structure. Thorough investigations were performed on the effect of homogenization treatment on the evolution of these particles using optical microscopy (OM), X-ray diffraction (XRD) analysis, field emission gun-scanning electron microscopy (FEG-SEM), electron probe microanalysis (EPMA) and differential scanning calorimetry (DSC) and the results were quantitatively analyzed. The dependence of the fractions of the particles in the structure on homogenization parameters was also investigated using various quantitative methods. In addition, a comprehensive investigation on the formation of Cr-, Zr-, and Mn-containing dispersoids which commonly co-exist in the AA7020 aluminum alloy was performed.

2. Experimental procedure and data processing

Cubic samples of 2 cm in size were cut from the centre of a direct-chill (DC) cast AA7020 ingot. The chemical compositions of the variants of the AA7020 alloy used in this study are shown in Table 2. Isothermal homogenization treatments were performed in a salt bath at temperatures of 390-550 °C for 2-48 h, as shown in Table 3. Following the heat treatments, the samples were quenched in water.

Element (Wt %)	Si	Fe	Cu	Mn	Mg	Zn	Ti	Cr	Zr	Al
N1	0.31	0.28	0.2	0.34	1.24	4.36	0.001	0.10	0.08	Bal.
N2	0.30	0.30	0.19	0.35	1.20	4.37	0.002	0.10	0.13	Bal.
N3	0.29	0.31	0.2	0.36	1.22	4.37	0.001	0.10	0.20	Bal.
Nominal composition	<0.35	<0.35	<0.2	0.05-0.5	1.0-1.4	4.0-5.0	Zr+Ti= 0.08-0.25	0.1-0.4	0.08-0.20	Bal.

Table 2. Chemical compositions of the AA7020 alloy variants used in this study

Temperature (°C)	Time (hours)
	2
390	4
430	8
470	16
510	24
550	32
	48

Table 3. Homogenization treatment conditions used in this study



Optical microscopy (OM) was performed using an OLYMPUS BX60M light microscope on the samples etched using Barker's etchant. Images were analyzed using the Soft Imaging Software (SIS) image processor. Three samples in each homogenization condition were prepared and the analysis was performed on two images with approximately 6.2 mega pixel image quality and the average values are reported. The differences between the measured data from different samples and different images are represented by error bars.

The samples were examined using field emission gun-scanning electron microscope (FEG-SEM). The optimum operating voltage and current were 10 kV and 1 nA, respectively. With these settings, dispersoids as small as 10 nm in diameter could be detected.

The SEM images of the GB particles after different homogenization treatments were quantitatively analyzed to investigate their dissolution during homogenization. 20 GB particles were analyzed in each case, and the width was measured and the average value calculated. During homogenization at high temperatures, i.e., 510 and 550 °C, some of the GB particles were completely dissolved in the structure. The dissolved GB particles were also considered in the calculation with a null width. The average initial number density of the GB particles in 20 micrographs of the structure was counted to be  $2 \times 10^9 \mu\text{m}^{-2}$ . The average number density of the GB particles after homogenization was also counted employing the same method and, if it was less than the average initial number density, indicating the full dissolution of some of the GB particles, a zero width was put into the calculations.

Discs having a diameter of 3 mm were punched from the samples and ground down to a thickness of less than 60  $\mu\text{m}$ , followed by electro-polishing in a solution of 30% nitric acid and 70% methanol cooled to -25 °C in a double-jet polishing unit at 20V.

Energy dispersive X-ray (EDX) analysis was performed with an analyzer attached to the FEG-SEM to determine the chemical compositions of the particles in the as-homogenized microstructures. In the case of small particles (< 500 nm), in order to keep the analysis volume in the EDX measurements as small as possible, the analysis was performed on TEM samples with an average thickness of 100 nm or less.

Electron Probe Microanalysis (EPMA) was performed using an electron beam with energy of 15 keV and beam current of 50 nA employing Wavelength Dispersive Spectrometry (WDS). The composition at each analysis location of the sample was determined using the X-ray intensities of the constituent elements after background correction relative to the corresponding intensities of reference materials. The thus obtained intensity ratios were processed with a matrix correction program CITZAF [43]. The points of analysis were located on lines with increments of 2  $\mu\text{m}$  and involved the elements of Cr, Mn, Cu and Zr. Al was measured by difference.

A BRUKER-AXS D5005 diffractometer with Cu  $K\alpha_1$  wavelength was used to identify the phases present in the as-cast and as-homogenized conditions. Quantitative XRD (QXRD) analysis was performed using the direct comparison method [44] to estimate the weight percent of the phases in the structure. Application of this method requires the weight percent of the phase of interest (i.e., GB particles) in the as-cast structure, as the baseline. To calculate the weight percent of the GB particles in the as-cast structure, the surface fraction of the GB particles was calculated using FEG-SEM together with EDX analysis. The analysis was performed on 20 images at a magnification of 1000 and all the particles present in each image were analyzed. Assuming a uniform distribution of the GB particles in the structure, the surface fraction can be approximated to be equal to the volume fraction. The volume fraction of the GB particles was converted to weight percent using the density of the GB

particles ( $3709 \text{ kg/m}^3$  [45, 46]) and the density of AA7020 aluminum alloy ( $2780 \text{ kg/m}^3$  [47]). The only assumption made was the density of the other particles (a mixture of various phases) other than the GB particles being equal to the density of the AA7020 aluminum alloy.

To determine the volume fraction of particles from the data obtained by optical and SEM microscopy, a simple rule was used. It was assumed that the average surface fraction measured in a large number of images from different positions in the substrate was representative of the volume fraction [48]. It has been mathematically proven that the average surface fraction is equal to the volume fraction, provided that an enough large number of sections are investigated [48]. In this research, the investigation was performed on such a number of images that a constant average value was obtained, being not significantly changed by adding another image to the measurements.

The number density and radii of dispersoids obtained from SEM micrographs are in the form of the number of particles on many cross sections in the observation area in 2-D. 2-D cross section observations of the volume generally do not directly correspond to the coherent values in 3-D. In other words, the average particle diameter and number density of particles in each size group of the size distribution are not correct representatives of the real numbers in 3-D. The reason is that the crossing plane may not cut the particle in the middle and therefore, an observed specific cross section with a constant size may be a cross section of a particle which is cut through the middle or a cross section of a larger particle which is not cut through the middle. This point is schematically illustrated in Fig. 4 [48]. It can be seen that a mono-dispersed system of diameter  $D_j$  in 3-D can result in different circular sections in 2-D. It is shown in Fig. 5 that particles of large sizes can contribute to increasing the 2-D observed number density of particles with smaller sizes depending on the geometry of the cutting plane.

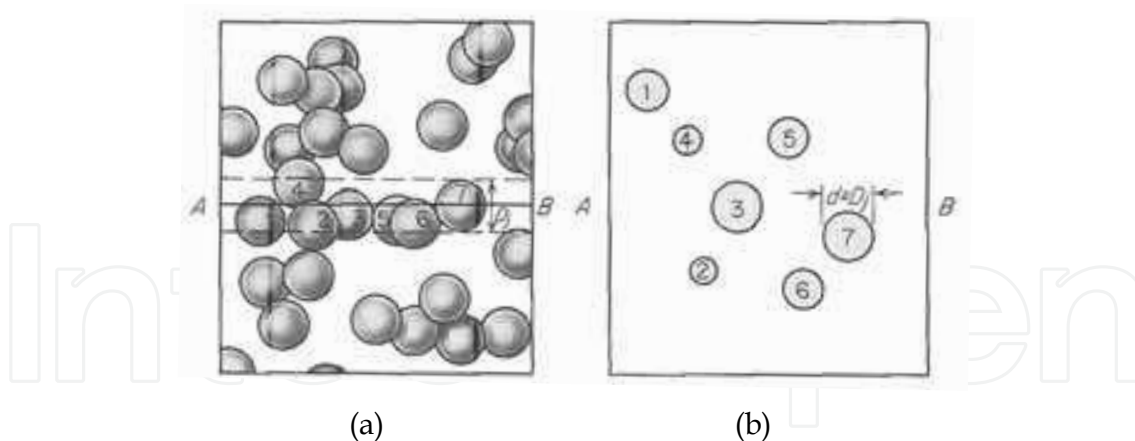


Fig. 4. (a) Distribution of mono-sized particles of  $D_j$  in 3-D and (b) observed A-B cross section of the particle distribution in 3-D [48]

The solution to this problem is to subtract the contribution of large particles to the 2-D measured sizes of smaller particles. For this purpose, different methods such as Scheil's method, Schwartz's method, Schwartz-Saltykov method have been proposed and used [48]. These methods can be used to find the distribution of particle sizes from a distribution of section diameters. The three methods differ in the details of how the numbers of sections contributed by larger spheres are determined.

In addition to the methods mentioned above, there are other methods which work with the distribution of section areas to determine 3-D particle sizes. Among these methods Johnson's and Johnson-Saltikov methods are well known. Johnson's derivation is applicable only to single-phase structures. However, Saltykov's improvement of Johnson's method applies to a distribution of particles as well as grain sizes [48]. Since the method is applicable for the prediction of grain and subgrain sizes in addition to particles, Johnson-Saltykov method was used in this research.

According to Saltykov's method [48], the most rational scale for the classification of particles (or grain sizes) is a linear logarithmic scale of diameter. Using the Johnson-Saltykov method, the analysis and calculations in the logarithmic scale can be simplified and facilitated. An advantage of this method is that a size distribution of particles can be obtained directly [48]. However, it must be noted that the resulting size distribution graphs will be presented by logarithmic size categories.

Thermal analysis of the as-cast and homogenized materials was carried out by means of a DSC analyzer at a heating rate of 20 °C/min over a temperature range of 35 to 700 °C. Samples were cubes weighing 12 mg each and  $\text{Al}_2\text{O}_3$  powder was used as the reference. The analysis was performed under the protection of Ar gas. To ascertain the effect of homogenization treatment on the dissolution of the LMP phases the DSC profiles were quantitatively processed. For this purpose, the area underneath the peak was correlated to the fraction of the LMP phases in the structure [3].

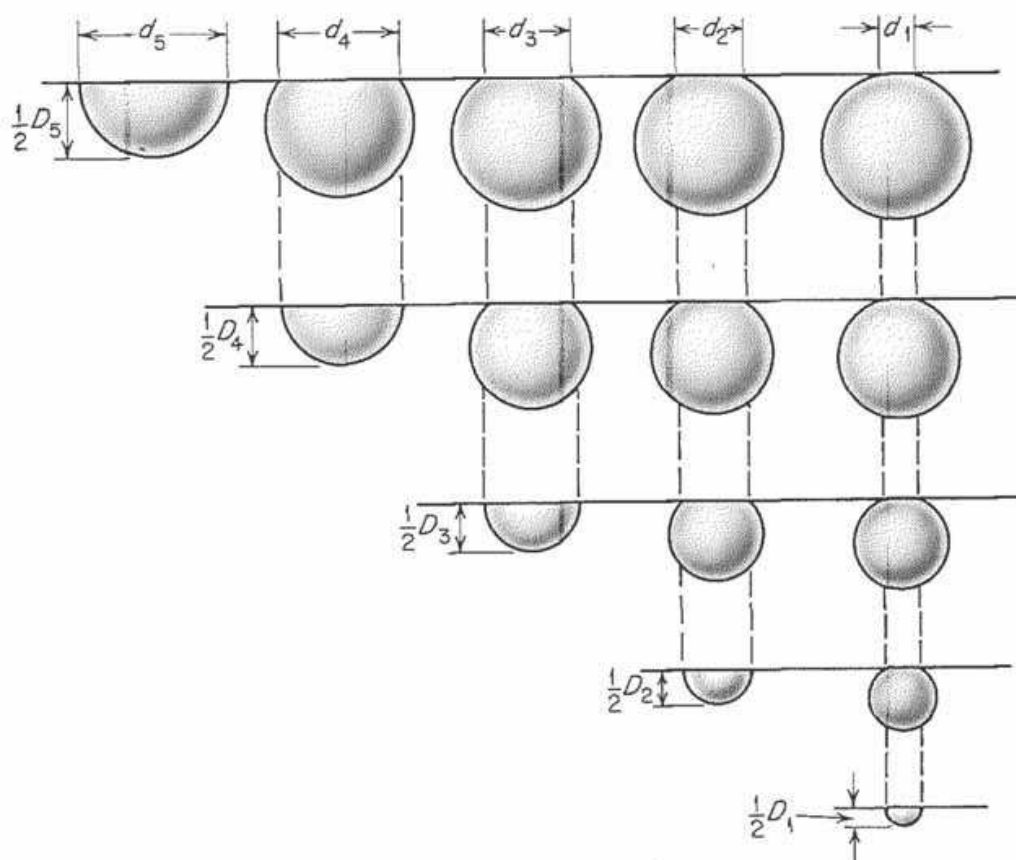


Fig. 5. Contribution of single size particles, i.e.,  $D_5$  in different 2-D size groups depending on the geometry of cutting plane [48]

### 3. The as-cast microstructure

#### 3.1 Grain boundary (GB) particles

Low and higher magnification secondary electron FEG-SEM images of the as-cast microstructure of an AA7020 aluminum alloy variant (N2) are shown in Fig. 6. The constitutive particles elongated along the grain boundaries can be clearly seen. The average width of these grain boundary (GB) particles is 640 nm. The perturbations on the surfaces of the GB particles are illustrated by arrows in Fig. 6 (b).

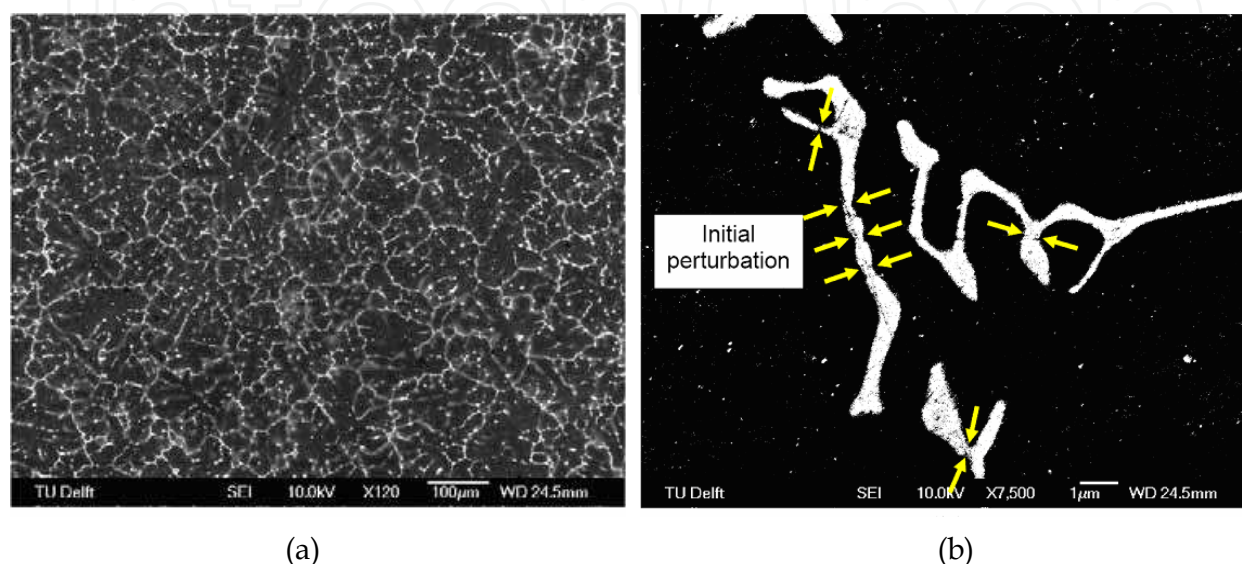


Fig. 6. (a) Low and (b) higher magnification SEM micrographs showing the GB particles in the as-cast microstructure (alloy variant N2) [49]

To determine the compositions of the GB particles, EDX analysis on more than 20 GB particles having the same morphology was performed. The results showed that the majority of the GB particles had similar compositions, as given in Table 4. By using an image analyzing software together with EDX analysis on a large number of different secondary phases in the as-cast structure, the initial fraction of the GB particles with respect to all of the secondary phases was calculated to be  $74 \pm 3$  wt.%.

With XRD analysis, a phase in a mixture can be identified if its volume fraction is higher than 5% [44]. The results of the image analysis indicated that the volume fraction of the GB particles was close to 7%. Therefore, it was possible to determine the identity of these particles using XRD analysis [44]. The results, shown in Fig. 7, illustrate that only one secondary phase could be detected, which was  $\text{Al}_{17}(\text{Fe}_{3.2}\text{Mn}_{0.8})\text{Si}_2$  (PDF No. 01-071-4015 [45]). Comparison of the XRD results with the EDX analysis, as given in Table 4, shows a good agreement.

The chemical composition of thermodynamically stable Al-Fe-Mn-Si compounds may be presented by  $\text{Al}_{16}(\text{Fe,Mn})_4\text{Si}_3$  or  $\text{Al}_{15}(\text{Fe,Mn})_3\text{Si}_2$  [4]. The crystallography of the intermetallic phases containing aluminum, silicon, iron and manganese implies that they should be considered as phases with multiple sublattices [50]. Therefore, these compounds may be simply considered as a solution of the Al-Fe-Si particles and Mn or vice versa. In this case, their formation and stability at different conditions obey the thermodynamics of solutions. Since Fe and Mn can reside on the same sublattices [50], the Al-Fe-Mn-Si particles can be considered  $\text{Al}_{16}(\text{Fe}_{(1-y)}\text{Mn}_y)_4\text{Si}_3$ . From the role of the  $RT((1-y)\ln(1-y)+y\ln y)$  term in the Gibbs



free energy of solutions [51], it can be stated that a compound with equal values of Fe and Mn has the lowest total free energy.

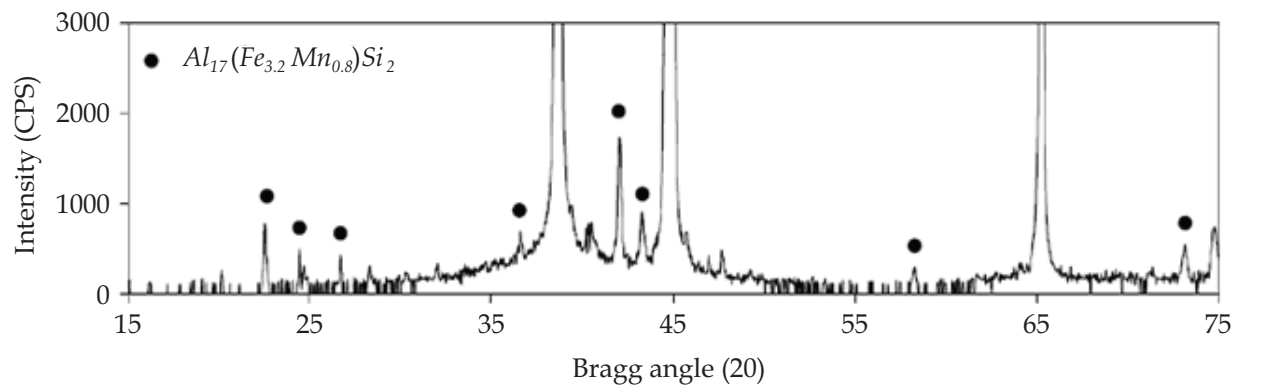


Fig. 7. X-ray diffraction pattern of the as-cast material showing the presence of the GB particles in the alloy variant N2 [49]

Element	Al	Fe	Mg	Si	Zn	Cu
EDX	72.1	16.1	2.8	4.3	2.7	2.0
XRD	62.2	24.2	6.0	7.6		

Table 4. Measured mean compositions (wt. %) of the grain boundary constitutive particles in the as-cast material (alloy variant N2) together with the calculated chemical compositions of the suggested phase identity based on the XRD analysis

In the DC-cast AA7020 aluminum alloy, the amount of Fe is larger than Mn in the grain boundary regions. The larger amount of Fe may be attributed to the partitioning coefficients of Fe and Mn, which result in severer microsegregation of Fe toward the grain boundaries and therefore, a higher concentration of Fe in these regions [52]. Fe has a small solid solubility in aluminum [52]. Therefore, the excess Fe rather than what is consumed in Al-Fe-Mn-Si particles must form other intermetallic compounds. In this case, if  $y=0.5$ , in addition to the thermodynamically stable  $Al_{16}(Fe_{(1-y)}Mn_y)_4Si_3$  phase, some separate Al-Fe-Si and Al-Fe particles are expected to form to consume the remaining insoluble Fe at the grain boundaries. However, as mentioned above, the solution formation results in a decrease in the Gibbs free energy of the system determined by the  $-RT((1-y)\ln(1-y)+y\ln y)$  term. Therefore, in this system, the stable Al-Fe-Mn-Si particles dissolve some of the excess Fe and form the meta-stable  $Al_{17}(Fe_{3.2}Mn_{0.8})Si_2$  particles and the remaining Fe incorporates in other intermetallic compounds. The amount of the Fe dissolved in the stoichiometric  $Al_{16}(Fe_{(1-y)}Mn_y)_4Si_3$  particles should be so much that the total energy of the system is minimized by the formation of  $Al_{17}(Fe_{3.2}Mn_{0.8})Si_2$ , Al-Fe-Si and Al-Fe particles. The same may be valid for the replacement of Si atom with exceeding Al in the compound from the stoichiometric values.

3.2 Low melting point (LMP) phases

The presence of the low melting point (LMP) phases in the as-cast structure was determined using DSC. The DSC profile of the as-cast structure is shown in Fig. 8. It is clear that there is

an endothermic reaction at 576 °C and the melting of the bulk sample occurs at 661 °C. In order to ensure that the endothermic peak is associated with the melting of the LMP phases rather than their dissolution, two samples were heated at 10 °C higher and lower than the reaction temperature, i.e., 566 and 586 °C, for 1 min. DSC analysis of these samples showed that, after these treatments, the endothermic reaction still occurred, which indicated that the 1 min treatment did not result in the dissolution of the corresponding phases.

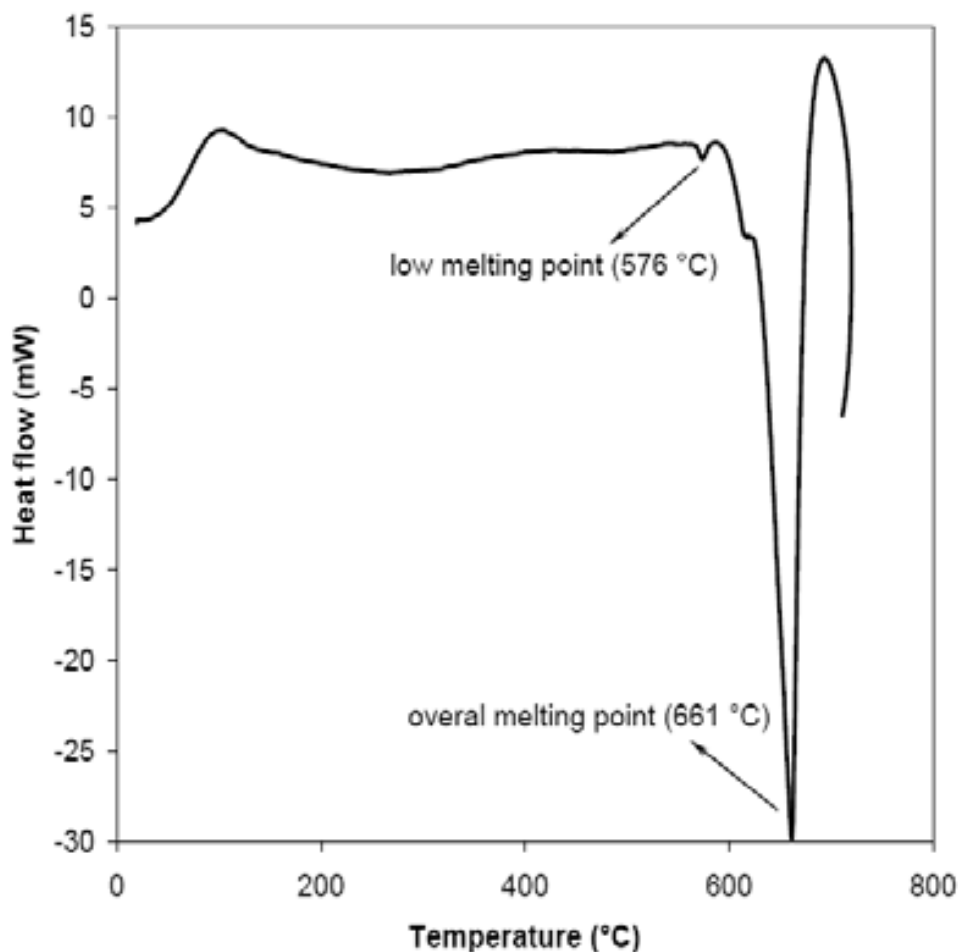


Fig. 8. DCS profile of the as-cast sample (alloy variant N2) at a heating rate of 20 °C/min [53]

The microstructures of the samples were investigated using field emission gun-scanning electron microscope (FEG-SEM). During the analysis, the phases in the as-cast structure, for example,  $\text{Al}_{17}(\text{Fe}_{3.2}\text{Mn}_{0.8})\text{Si}_2$  and  $\text{Al-Fe-Si}$ , were detected whose compositions and morphologies were the same as those present in the as-cast structure. The only difference observed in the structures was that for the sample treated at 586 °C for 1 min, the morphology of the Al-Cu-Mg-Zn particles changed from a round shape in the as-cast structure, shown in Fig. 9 (a), to a sponge-like one with perturbations as shown in Fig. 9 (b). These morphological changes must be due to the melting of Al-Cu-Mg-Zn particles during heating up to 586 °C and re-solidification of the particles upon water quenching. This suggests that the endothermic reaction observed in the DSC profile is indeed due to the melting of Al-Cu-Mg-Zn particles. The primary elements present in the LMP phases and their concentrations are shown in Table 5, based on the EDX analysis.

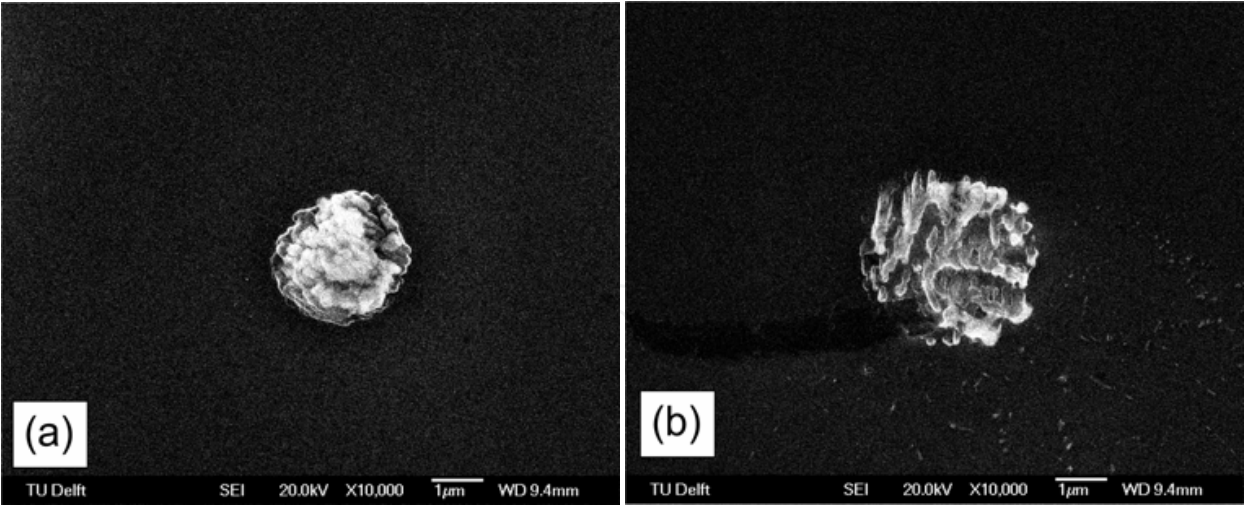


Fig. 9. (a) An Al-Cu-Mg-Zn particle with a round shape in the as-cast structure and (b) a sponge-like Al-Cu-Mg-Zn particle with perturbations in sample N2 after heating to 586°C for 1 min and water quenching [53]

Element	Al	Cu	Mg	Zn
wt%	57±7	17±3	8±2	6±2

Table 5. Measured mean composition of the Al-Cu-Mg-Zn particles in the as-cast alloy variant N2

4. Effects of homogenization

4.1 Microstructural evolution during homogenization

Fig. 10 shows the optical microstructures of the material (alloy variant N2) after 2 h homogenization at different temperatures. Homogenization at 390 and 430 °C led to an increase in the volume fraction of particles. At 470 °C, the volume fraction appeared to be unchanged, while at 510 and 550 °C, it decreased.

Fig. 11 shows low and higher magnification secondary electron FEG-SEM images of the dominant particles formed during homogenization at 390 °C. The grain boundaries are still delineated by the GB particles while the initial continuity of the GB particles shown in Fig. 6(a), is deteriorated by spheroidization. Moreover, large needle-shaped and round precipitates appear in the structure. Examples of these precipitates together with large Al-Fe-Si particles are illustrated in Fig. 11(b). These particles, as pointed at in Fig. 11(a), are dispersed inside the grains. EDX analysis on more than 20 particles with similar morphologies determined the chemical compositions of these precipitates and the results are shown in Table 6.

It was possible to identify these compounds formed during homogenization at low temperatures using XRD analysis. The results given in Fig. 12 (a) show that in addition to the previously present GB particles (Fig. 7), new particle are present in the homogenized microstructure, i.e.,  $MgZn_2$  ( $\eta$ ) and  $Mg_2Si$  ( $\beta$ ) particles. However, the XRD pattern of the sample homogenized at 550 °C, presented in Fig. 12 (b), shows that no new particles have been formed during homogenization at such a high temperature, which is consistent with the results from the optical microscopy analysis, shown in Fig. 10.

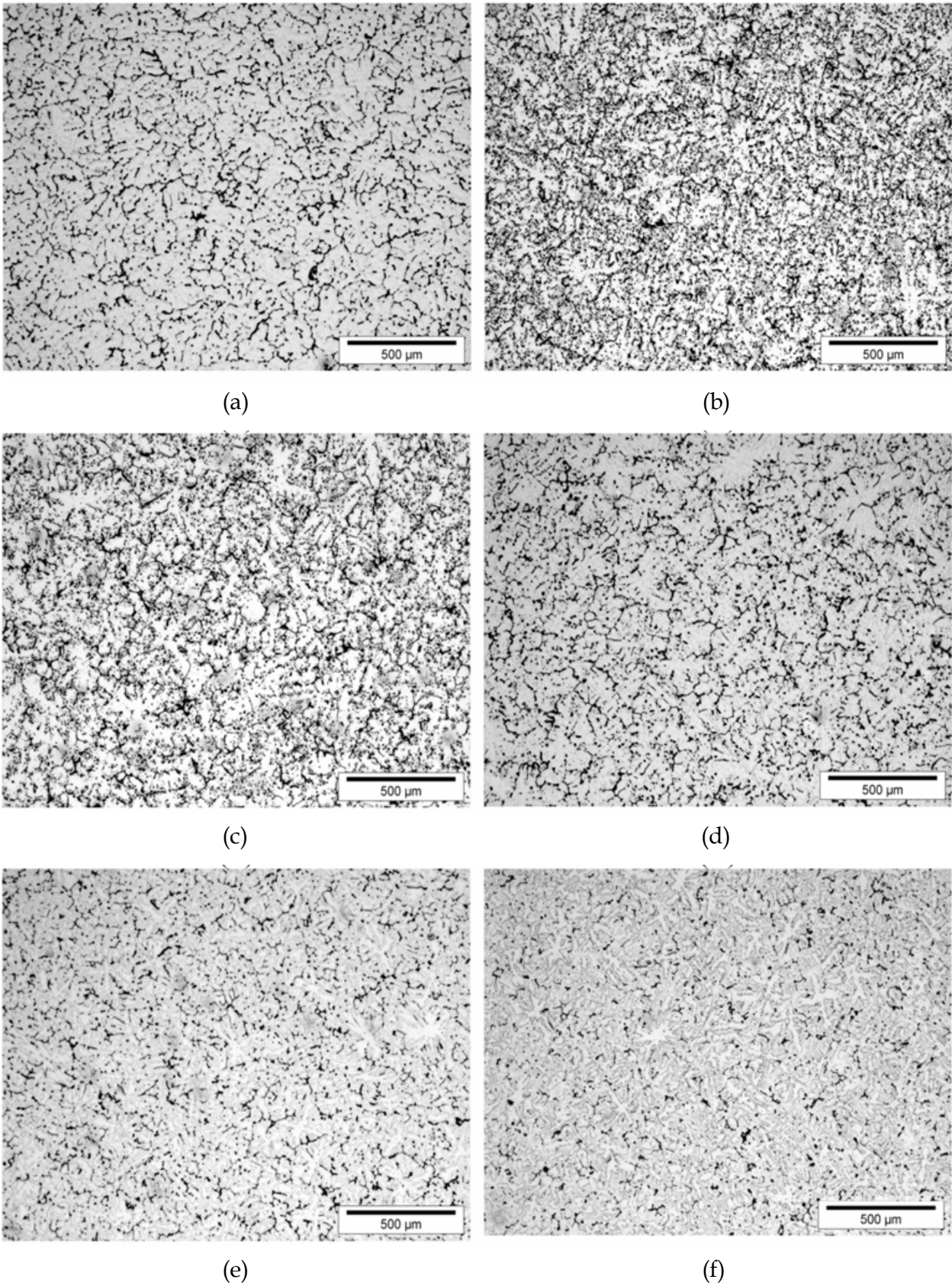


Fig. 10. Effect of the temperature of homogenization for 2 h on the evolution of particles in alloy variant N2, (a) the initial structure, (b) 390, (c) 430, (d) 470, (e) 510 and (f) 550 °C [49]



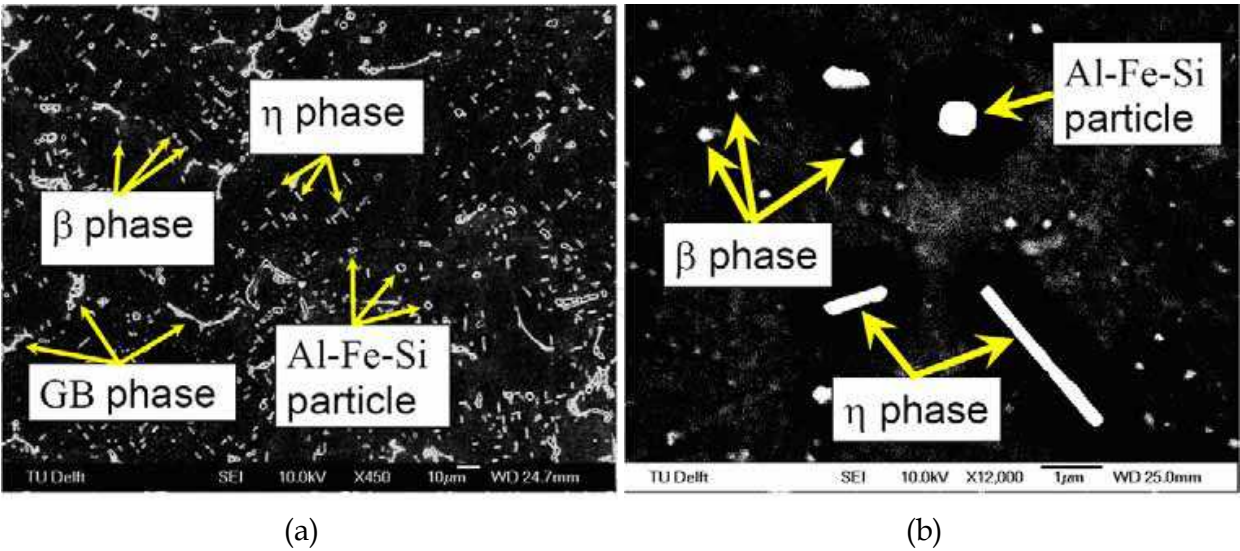


Fig. 11. (a) Low magnification FEG-SEM image of the alloy variant N2 homogenized at 390 °C, showing the GB particles and (b) the needle-shaped and round  $\text{MgZn}_2$  ( $\eta$ ) and  $\text{Mg}_2\text{Si}$  ( $\beta$ ) particles together with large Al-Fe-Si particles [49]

Element (Wt%)	Al	Mg	Zn	Si	Fe
$\eta$ phase (EDX)	63±4	4±2	28±1	3±1	2±1
$\eta$ phase (XRD)	...	15.7	84.3	...	...
$\beta$ phase (EDX)	56±4	22±3	5±2	15±3	2±2
$\beta$ phase (XRD)	...	63.38	...	36.62	...

Table 6. Measured mean compositions (wt. %) of the needle-shaped and round precipitates in the as-homogenized microstructure of the alloy variant N2 together with the stoichiometric chemical compositions based on the XRD results

It was also found that even after homogenization at a high temperature, i.e., 550 °C, some of the particles were not dissolved in the structure. These retained particles are mostly the GB particles and other particles which together with their EDX spectrums are shown in Fig. 13 (a) and (b). EDX suggested that the particles shown in Fig. 13 (a) and (b) were  $\text{Al}_{13}\text{Fe}_4$  and  $\text{Al}_8\text{Fe}_2\text{Si}$ , respectively.

The investigations carried out using the FEG-SEM of the samples homogenized at 390 and 430 °C indicated the presence of needle-shaped and round precipitates, as shown in Fig. 11. The morphologies of these particles and their chemical compositions indicated these particles to be  $\text{MgZn}_2$  and  $\text{Mg}_2\text{Si}$  precipitates, which is in agreement with [54-56]. The formation of these precipitates may be attributed to the super-saturation of the structure with alloying elements occurring during solidification at high cooling rates applied during DC casting. When the as-cast alloy is exposed to a homogenization treatment at a low temperature (< 470 °C), there is a tendency for the alloying elements to precipitate out. As the temperature increases (> 470 °C), the solubilities of these elements in the  $\alpha$ -Al matrix

increase [4, 57] and the formation of new particles is not expected. Thus, it can be concluded that the formation of new particles or the dissolution of old ones depend primarily on the homogenization temperature.

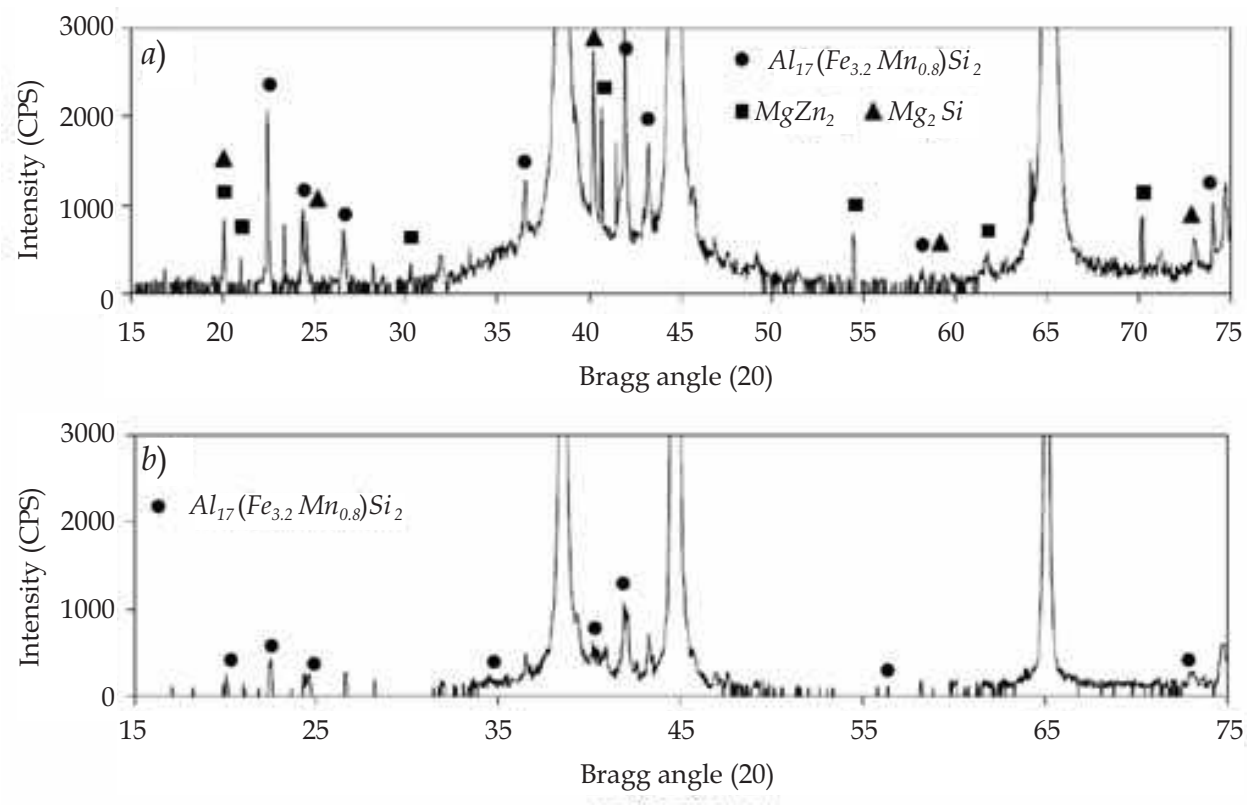


Fig. 12. X-ray diffraction patterns of the alloy variant N2 homogenized at (a) 430 and (b) 550 °C showing the presence of the GB particles,  $MgZn_2$  ( $\eta$ ) and  $Mg_2Si$  ( $\beta$ ) particles [49]

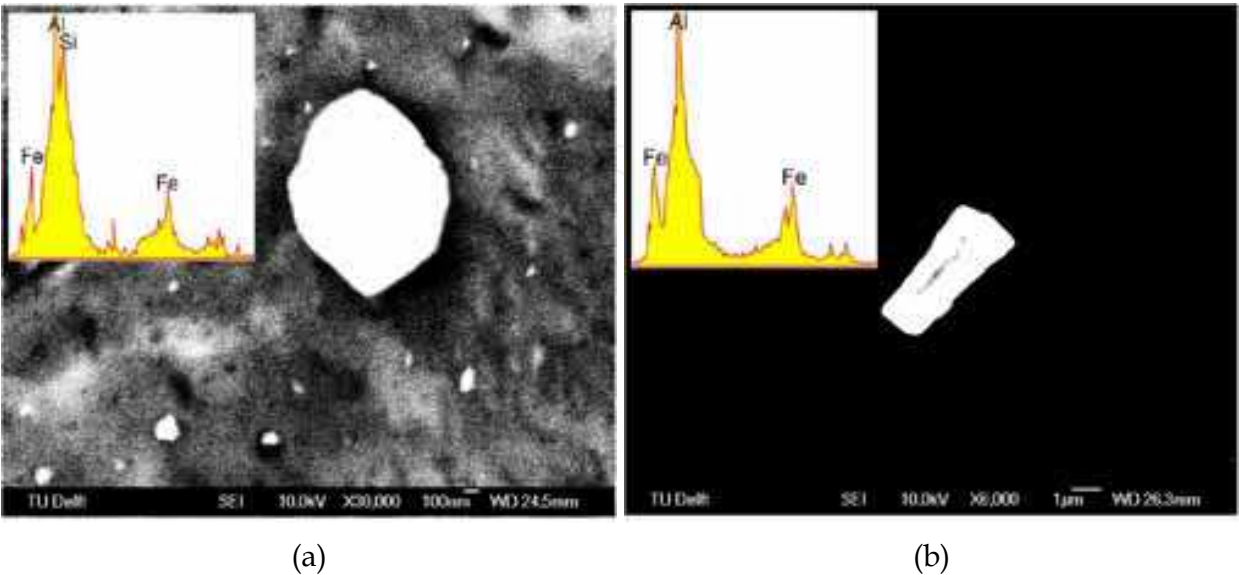


Fig. 13. Particles remaining in the microstructure of the alloy variant N2 after homogenization at 550 °C for 48 h, (a)  $Al_8Fe_2Si$  and (b)  $Al_{13}Fe_4$  particle [49]

#### 4.2 Evolution of the GB particles during homogenization

The evolution of a typical GB particle during homogenization at 390 and 550 °C is shown in Figs. 14 and 15, respectively. It is clear that the dominant process at lower temperatures is the spheroidization of the GB particle, while at higher temperatures the decrease in the width of the GB particle is the main evolution process.

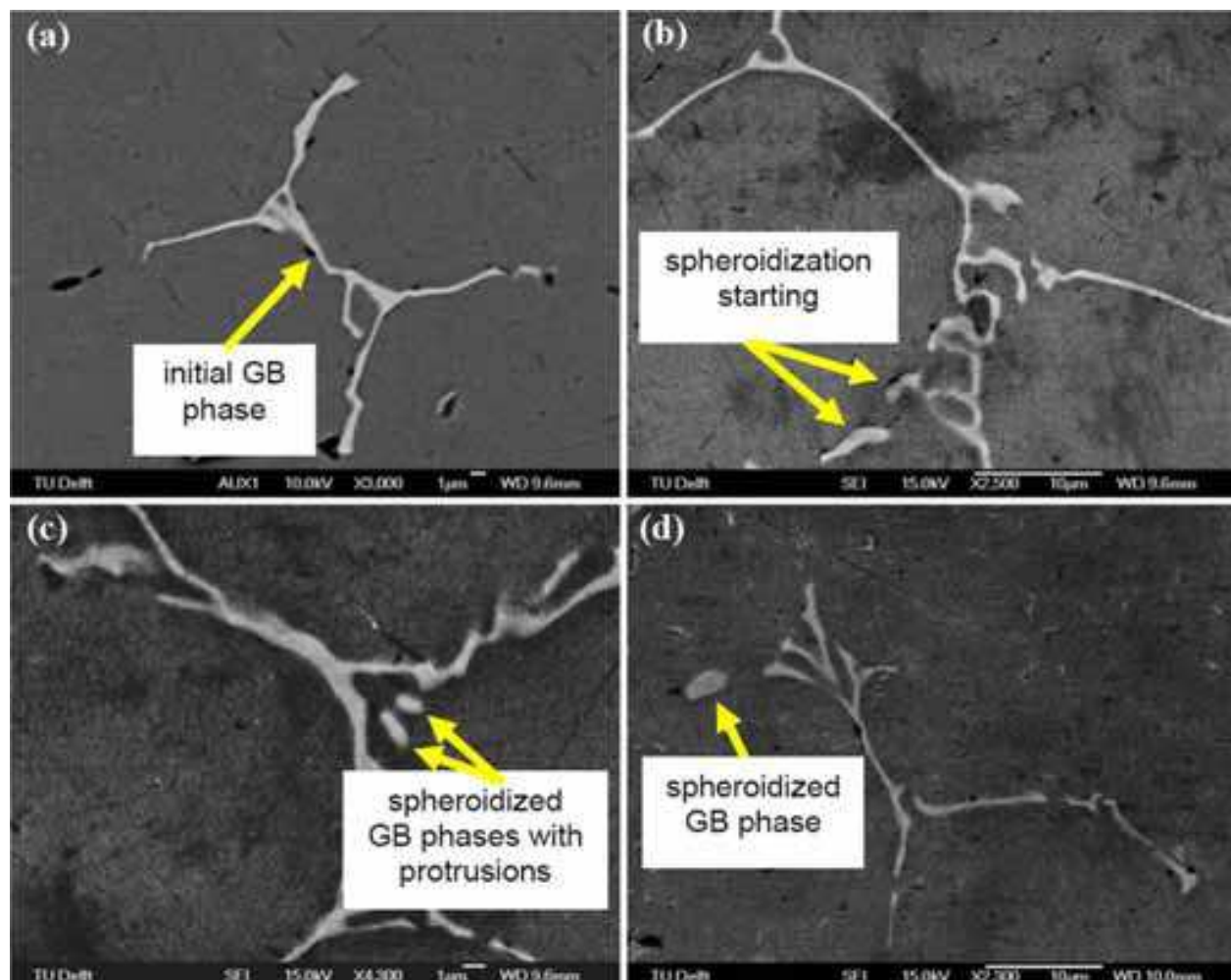


Fig. 14. Typical shapes of the GB particle after homogenization of the alloy variant N2 at 390 °C, (a) initial, (b) 2, (c) 8 and (d) 24 h [49]

Unlike the evolution of other particles in aluminum alloys [2, 14, 15], the evolution of the GB particles during homogenization, depending on the process parameters and the nature of the particles, may occur in the form of spheroidization or dissolution. The spheroidization mechanism of these particles is quite interesting. However, more interestingly, the dissolution of the GB particles obeys a specific dissolution mechanism introduced hereafter as the thinning, discontinuation and full dissolution (TDFD) mechanism.

##### 4.2.1 Spheroidization during homogenization at low temperatures

The analysis of the SEM images indicates that although the fraction of the GB particles does not decrease during homogenization at 390 °C, the morphological changes towards spheroidization take place, as can be seen in Fig. 14. The analysis of 20 pictures from the as-



cast structure and the one homogenized at 390 °C for 48 h indicates that after homogenization the fraction of spheroidized particles increases by two times compared with the as-cast structure.

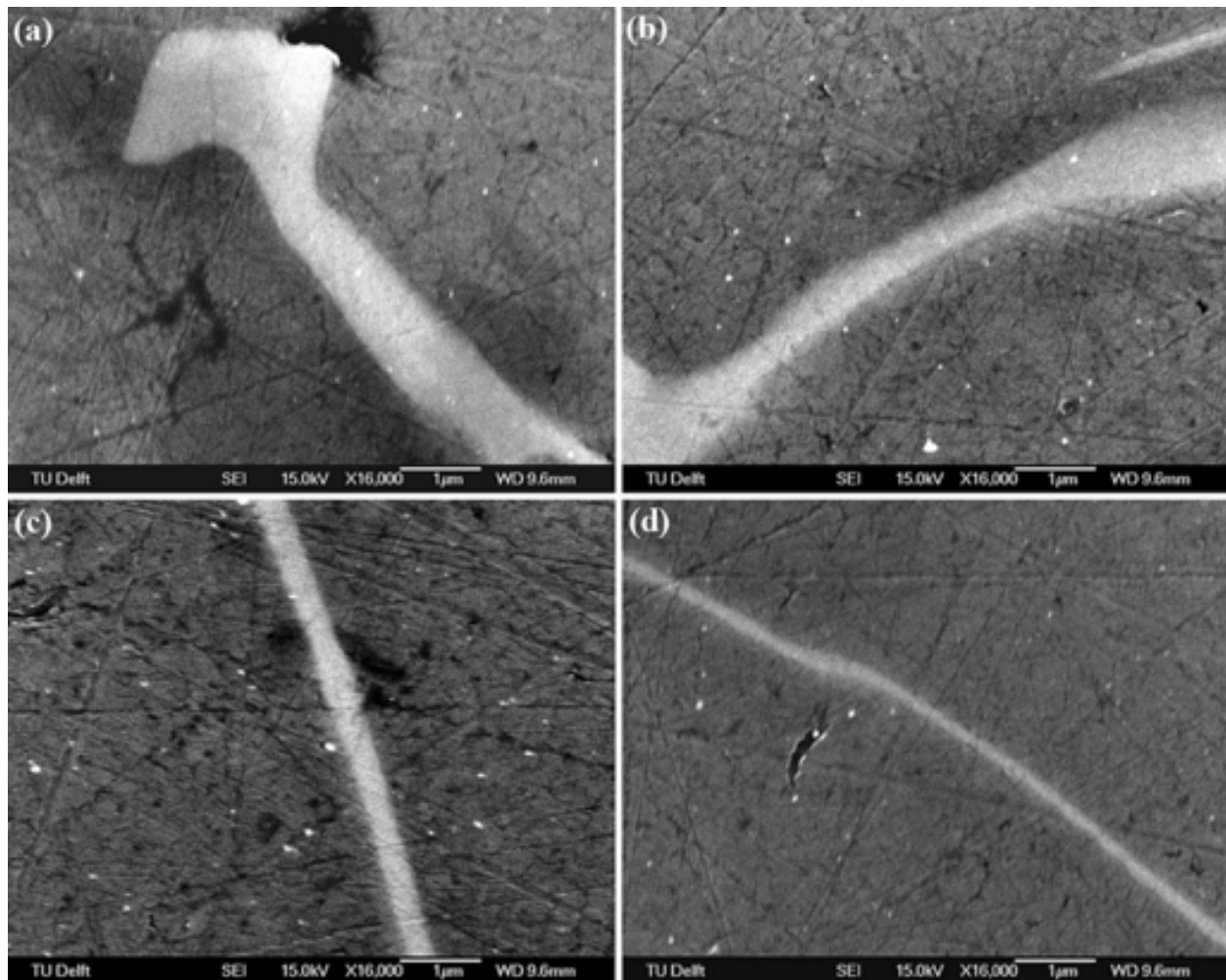


Fig. 15. Decrease in the width of a GB particle after homogenization of the alloy variant N2 at 550 °C, (a) initial, (b) 2, (c) 8 and (d) 24 h [49]

The proposed mechanism of the spheroidization of the GB particles is illustrated in Fig. 16, based on the experimental observations from the FEG-SEM images (a typical one is shown in Fig. 14). Fig. 16(a) shows a GB particle with initial protrusions on its surface. Afterwards, spheroidization occurs and the GB particle takes an ellipse shape, Fig. 16(b). The spheroidization continues till the GB particle takes a spherical shape with protrusions on its surface, Fig. 16(c), and the process ends with removing the protrusions till the GB particle resembles a sphere, Fig. 16(d). The driving force for spheroidization is the decrease in the surface energy of the GB particle with decreasing interfacial length between the GB particle and the aluminum matrix [15, 58].

As mentioned earlier, one of the main aims of homogenization treatment prior to hot deformation is to dissolve detrimental particles, especially those located at the grain boundary regions. Although this goal would not be achieved if the particles are not dissolved but spheroidized, spheroidization of particles can be beneficial in the sense that



these particles cause less stress concentrations at sharp tips and edges and therefore, inhibit crack initiation which can lead to an improvement in the hot workability of the material.

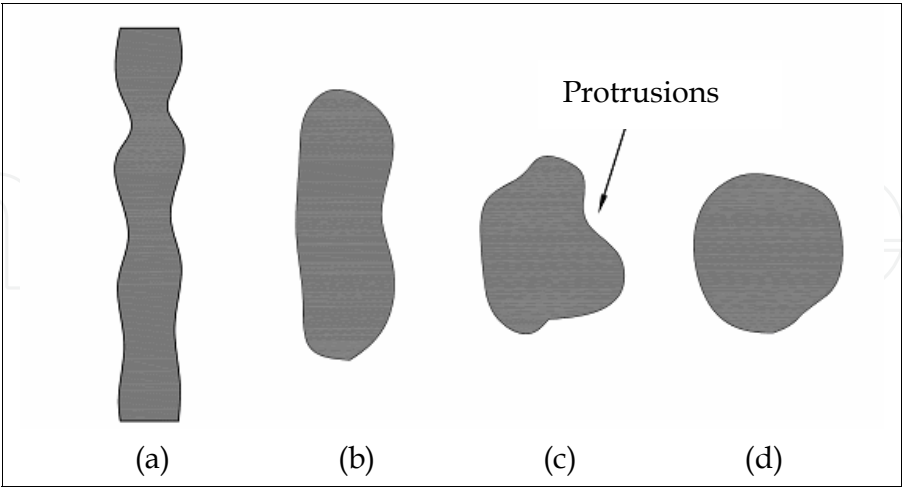


Fig. 16. Schematic view of the spheroidization mechanism describing the evolution of a GB particle during homogenization [49]

**4.2.2 Thinning, discontinuation and full dissolution (TDFD) during homogenization at high temperatures**

In order to understand the dissolution sequence of the GB particles at high homogenization temperatures, the evolution of a GB particle was investigated at different time intervals during homogenization at 550 °C. It was found that the dissolution process started with the thinning of the GB particle without primary spheroidization. Fig. 15 shows that the average width of the GB particle decreases from 640 nm to 130 nm by a homogenization treatment at 550 °C for 24 h. The thinning process continues until the GB particle become discontinuous in some regions (Fig. 17) and finally the full dissolution of the GB particles occurs. The occurrence of discontinuities during spheroidization of an eutectic particle has been reported elsewhere, for example in [59].

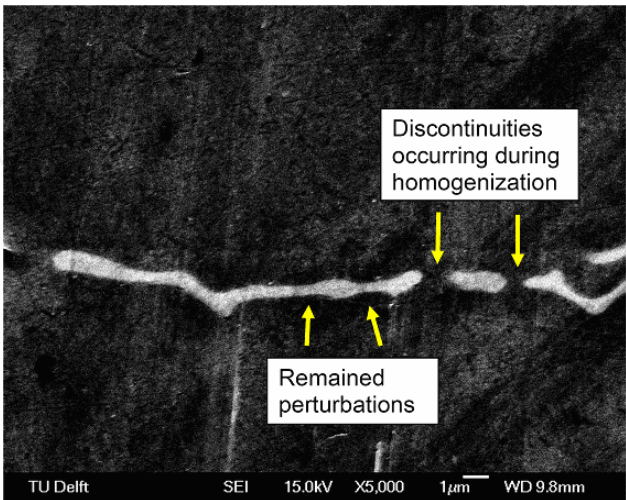


Fig. 17. A GB particle after homogenization at 550 °C for 8 h, showing the thinning and discontinuation (alloy variant N2)

The dissolution mechanism of a GB particle at different stages is schematically illustrated in Fig. 18. The driving force is the increases in the solubility limits in the matrix at high temperatures and therefore the presence of concentration gradients of Mn, Fe and Si in the structure. Fig. 18(a-c) schematically illustrates the overall thinning process of a GB particle. Assuming that during homogenization an overall decrease in the width of a GB particle occurs at a constant rate in different regions regardless of the widths, Fig. 18(a) through (c), the parts having smaller widths meet each other sooner than other parts, as shown by arrows in Fig. 18(d). Therefore, the discontinuities, Fig. 18(e), occur as a result of the inherent perturbations, Fig. 6(b), of the surfaces of the GB particle, shown by arrows in Fig. 18(a). Afterwards, the dissolution continues with the same mechanism as occurring to the small parts till the GB particle disappears. The remaining perturbations which help the continuation of dissolution of the GB particle with a similar mechanism are shown by arrows.

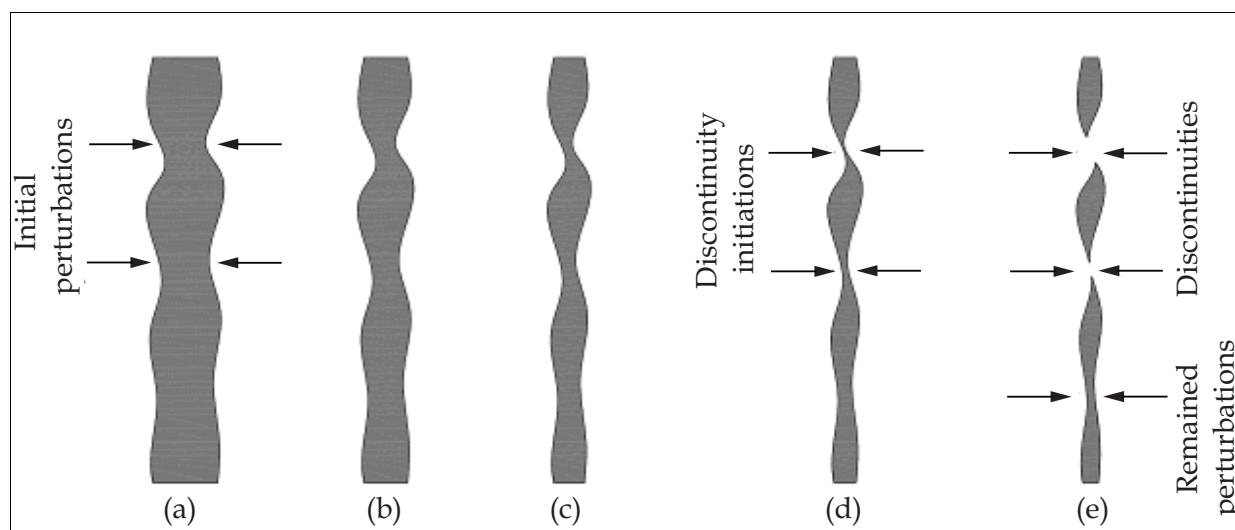


Fig. 18. Schematic description of the thinning, discontinuation and full dissolution (TDFD) mechanism responsible for the evolution of a GB particle during homogenization at high temperatures [49]

The experimental observations of the shapes of the particles, presented in Fig. 19, show that the tips of the particles may initially have rectangular, ellipsoidal, needle or circular cross sections, Fig. 19(a) through (c). However, as shown in Fig. 19(d) through (f), during the dissolution, the tips get a circular cross section. Assume the initial shape of the tips to be rectangular having two steep tips at the edges. According to the Gibbs-Thompson equation [15], a large concentration of the solute at the interface is resulted in, which indeed increases the dissolution rate significantly. The steep edges dissolve sooner and therefore a circular tip will be produced. The same is valid for an ellipsoidal cross section.

## 5. Quantitative analysis of particle dissolution

### 5.1 All the particles

#### 5.1.1 Results of quantitative optical microscopy (QOM)

Fig. 20 shows the effect of homogenization time on the volume fraction of all the particles present in the structure. The calculation was based on the changes in the volume fraction of the particles in the structure, as shown in Fig. 10. It is clear that during homogenization at

390 and 430 °C the fraction of particles increases, while during homogenization at 510 and 550 °C the fraction of the particles decreases, indicating dissolution.

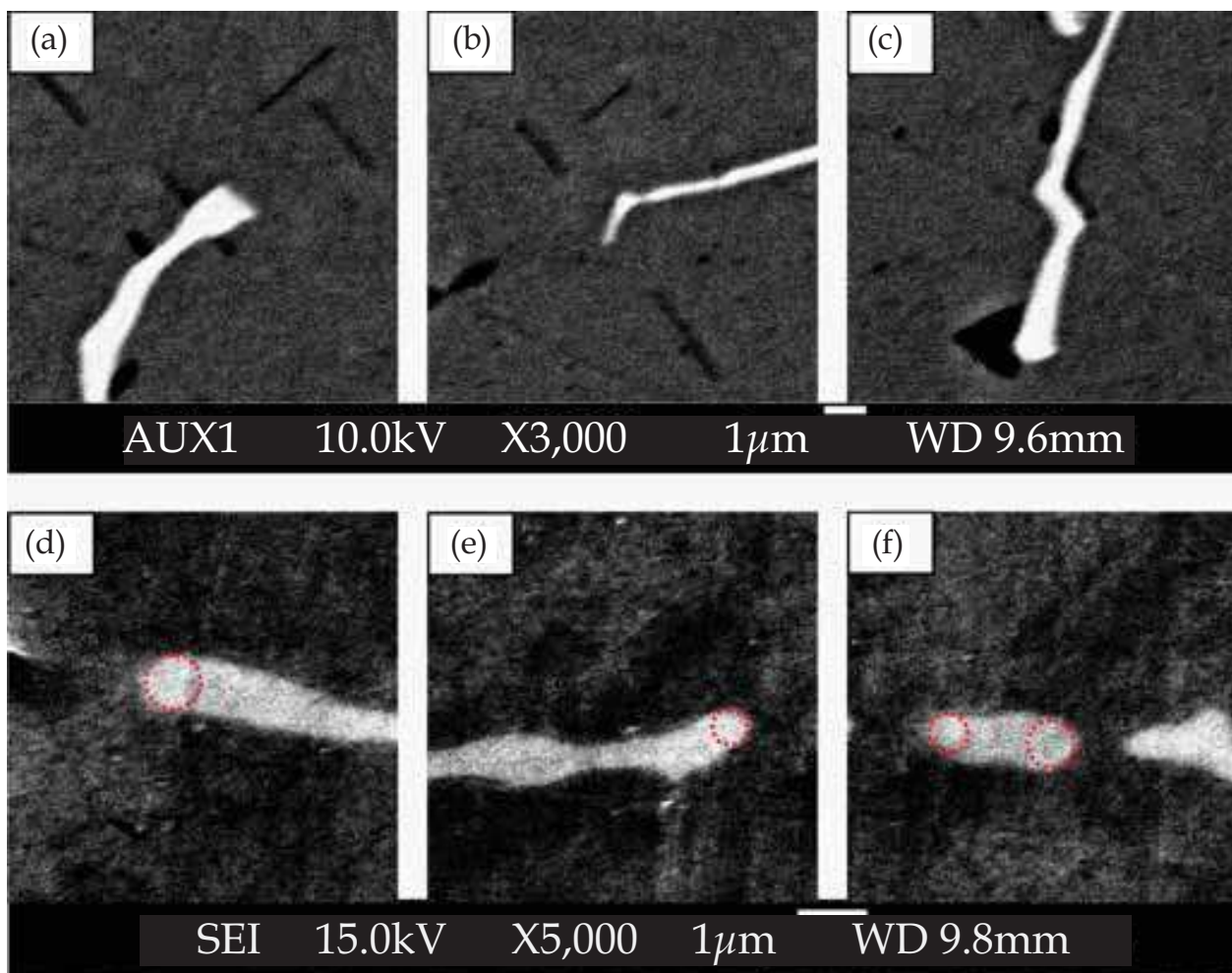


Fig. 19. Shapes of the tips of an  $\text{Al}_{17}(\text{Fe}_{3.2}\text{Mn}_{0.8})\text{Si}_2$  particle in the alloy variant N2, (a) through (c) in the initial structures and (d) through (f) after homogenization at 550 °C for 8 h. In (d) through (f), circles have been drawn on the tips of the particles, showing the perfectness of the circular cross section of the tips [60]

The most noticeable in Fig. 20 is the increase in the fraction of all the particles at the initial stage of homogenization at low temperatures, which acts in contrary to the aim of the homogenization process [2, 14, 15]. The increases in the fraction of particles during the first 2 h of homogenization at 390 and 430 °C, as shown in Fig. 20, are due to the formation of a large number of new particles, namely  $\text{MgZn}_2$  ( $\eta$ ) and  $\text{Mg}_2\text{Si}$  ( $\beta$ ). As stated above, it indicates that part of the elements precipitate out by forming precipitates during the first 2 h of homogenization.

## 5.2 GB particles

### 5.2.1 Results of quantitative XRD analysis (QXRD)

Fig. 21 compares the strongest XRD peaks and other ones related to the GB particles in the AA7020 alloy variant N2 samples homogenized at different temperatures for 8 h. This figure was obtained by focusing on the 41 to 44 ° Bragg's angle ( $2\theta$ ) range in the XRD patterns, i.e.,

Figs. 7 and 12. Compared with the as-cast structure, it is obvious that the intensity of the peaks related to the GB particles in the sample homogenized at 390 °C is almost unchanged, while at 430 and 470 °C it is decreased slightly. Homogenization treatment at higher temperatures, namely 510 and 550 °C, however, resulted in marked decreases in the intensity of the peaks related to the GB particles in the XRD pattern in comparison with that of the as-cast structure.

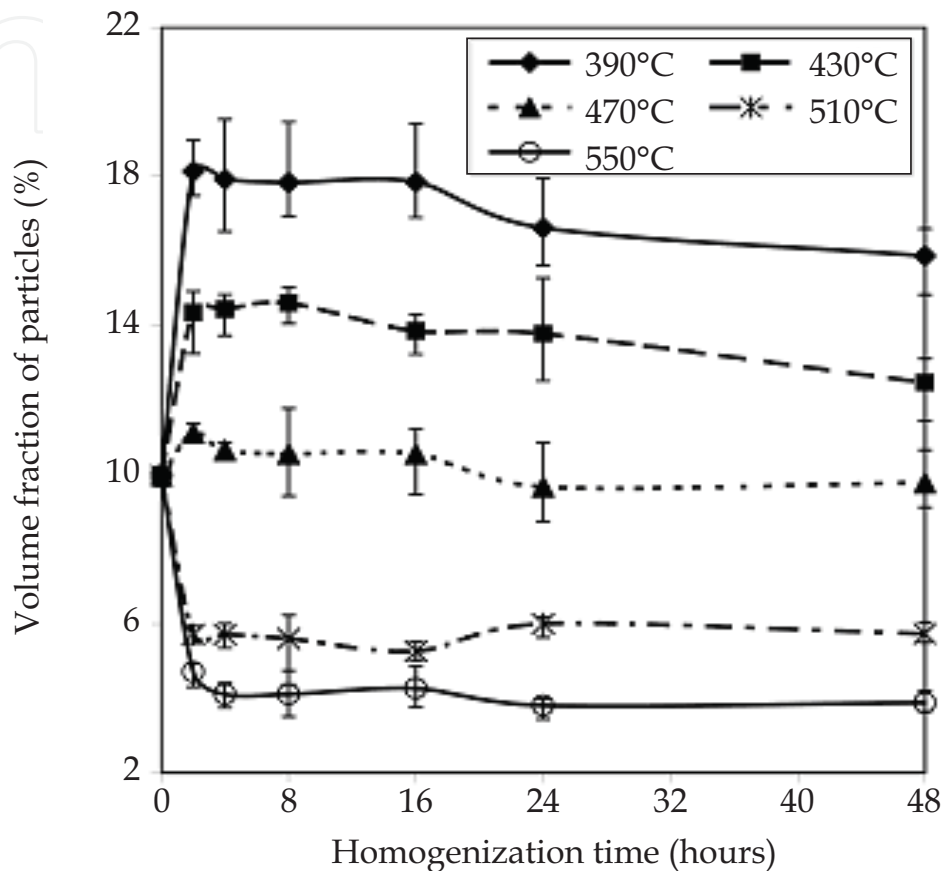


Fig. 20. Effect of homogenization time on the volume fraction of particles (alloy variant N2) [49]

To quantify the results, the fraction of the GB particles in the structure after homogenization was calculated according to the results of the XRD analysis using the direct comparison method [44]. As it was mentioned earlier, the initial fraction of the GB particles with respect to all of the secondary phases in the as-cast structure, necessary to form a baseline for the direct comparison method, was calculated to be  $74 \pm 3$  wt.%. Fig. 22 illustrates the weight percents of the GB particles as a function of homogenization time at different temperatures. It can be seen that the fraction of the GB particles after homogenization at 390 °C remains unchanged and at 430 °C it is decreased slightly, which is not in agreement with the results of the quantitative optical microscopy (QOM) shown in Fig. 20. Therefore, the increase in the fraction of particles during homogenization shown in Fig. 20 is due to the formation of new precipitates ( $\eta$  and  $\beta$ ), but not due to the increase in the GB particles. However, at higher temperatures, the fraction of the GB particles decreases, which is in line with the behavior shown in the optical microscopy measurements.



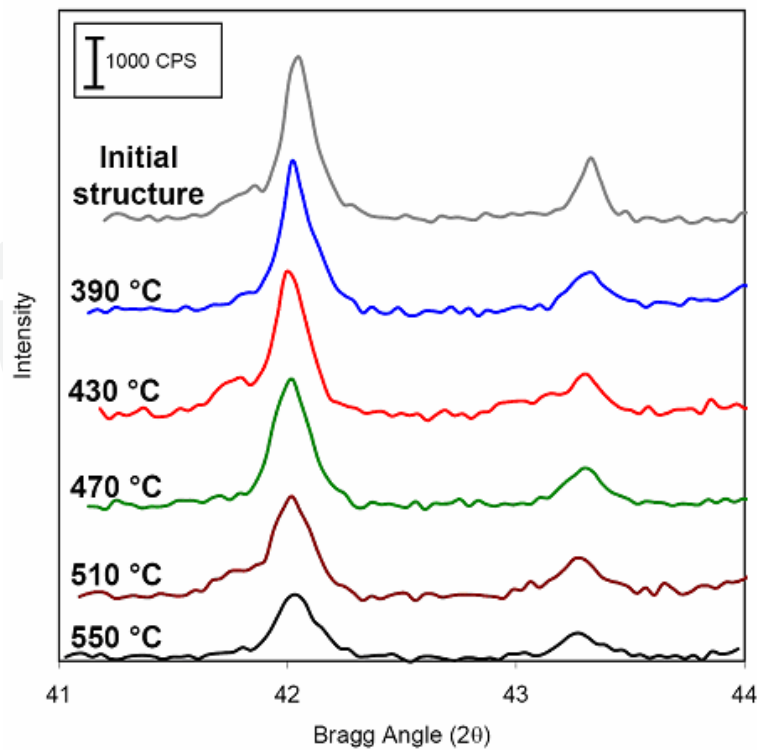


Fig. 21. The strongest (left) and another (right) XRD peaks related to the GB particles in samples homogenized at different temperatures for 8 h (alloy variant N2) [49]

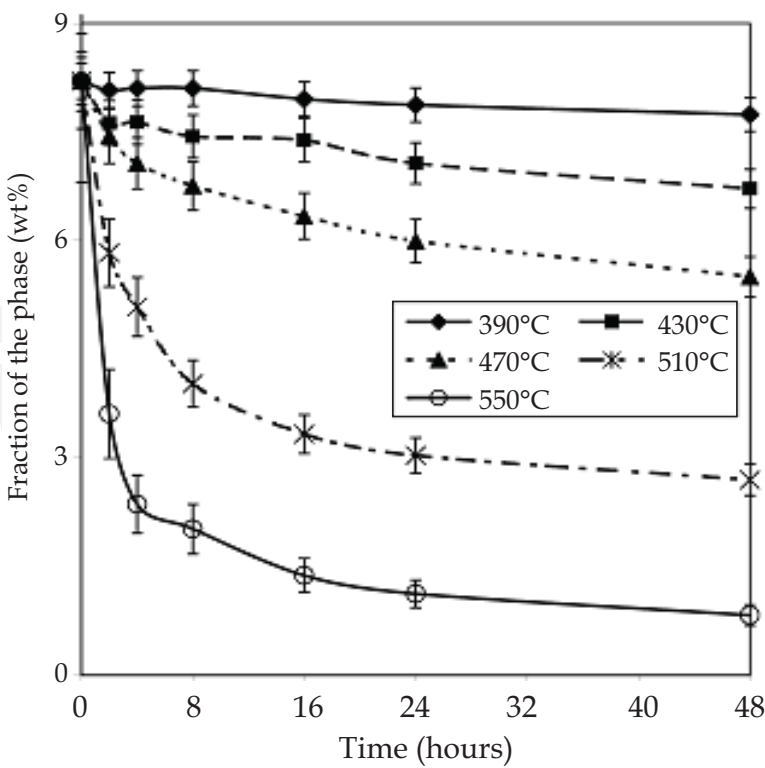


Fig. 22. Fraction of the GB particles (wt.%) in the structure of the alloy variant N2 after homogenization at various temperatures, based on the QXRD analysis [49]

### 5.2.2 Results of quantitative analysis using FEG-SEM (QSEM)

The measured average widths of the GB particles as a function of homogenization time are shown in Fig. 23. It can be seen that, at 390 and 430 °C, the average width of the GB particles is almost unchanged from the initial value. The minor variations in the width of the GB particles at these temperatures are within the margin of error. However, at higher temperatures, dissolution occurs, evidenced by the decreases in the width of the GB particles. It can also be seen in Fig. 23 that the most rapid dissolution occurs at the first few hours of homogenization regardless of homogenization temperature. Moreover, the dissolution rate is much higher at 550 °C.

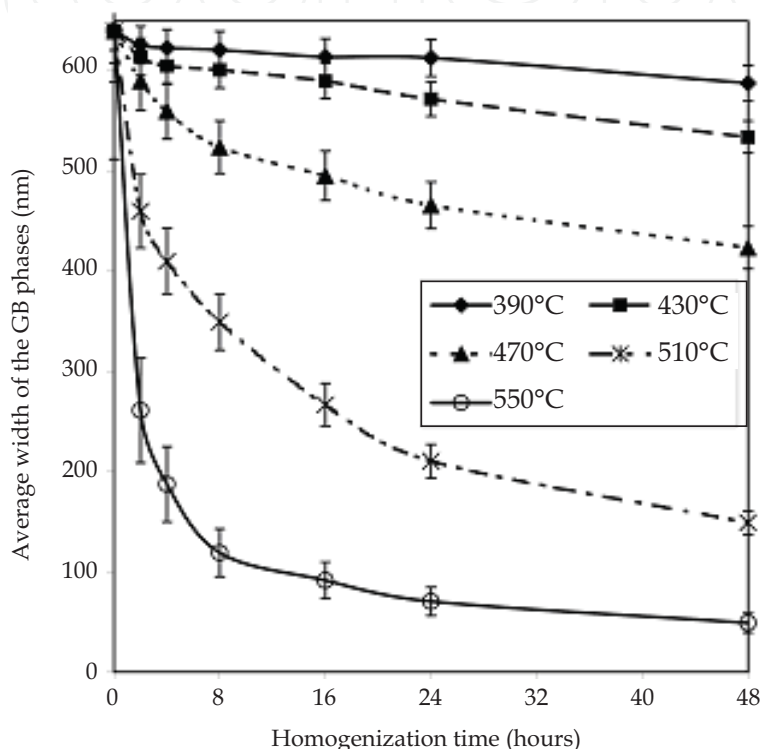


Fig. 23. Average GB widths in the alloy variant N2 as a function of homogenization time, based on the QSEM analysis [49]

To account for the dissolution of the GB particles, a study on the solubility limits of the elements composing the main GB particles, namely Fe, Mn and Si, is essential. The data on the solubility limits of the elements in Al-Mn-Fe-Si are scarce in the literature [4]. In this case, the solubilities of the elements in Al in the four-component Al-Mn-Fe-Si regions adjacent to the ternary systems may be estimated, based on three-component regions of the Al-Fe-Mn, Al-Fe-Si and Al-Mn-Si ternary systems [4]. Table 7 shows the solid solubility limits of iron, manganese and silicon in the four component Al-Fe-Mn-Si system at different temperatures [4]. It is clear that at low temperatures, i.e., lower than 470 °C, the solubility limits of the elements forming the GB particles are small in the  $\alpha$ -Al matrix. Therefore, considerable dissolution of the GB particles is not expected at these temperatures. This is in agreement with the results of the quantitative image analysis of the OM images, presented in Figs. 20, 21 and 22. At higher temperatures, however, the solubility limits increase, as shown in Table 7, which indicates that the most of the alloying elements in the GB particles are dissolved in the  $\alpha$ -Al matrix. It is also clear that even at such high temperatures (e.g., 550

°C), the solubility limits of the elements in the Al matrix are less than the weight percentages of those elements in the composition of the alloy (N2). Therefore, complete dissolution of all the GB particles is not expected even after holding for a long time. This explains the observations in Fig. 10 (f) and 15 (d) that there are still some GB particles remaining in the structure after homogenization at 550 °C. EDX analysis confirmed the existence of these particles even after homogenization at 550 °C for 48 h.

T (°C)	Solubility limit Wt%		
	Fe	Mn	Si
390	0.002	0.026	0.03
430	0.004	0.05	0.06
470	0.009	0.15	0.08
510	0.016	0.25	0.11
550	0.044	0.44	0.2

Table 7. Solid solubility limits of iron, manganese and silicon in the four component Al-Fe-Mn-Si system at different temperatures [4]

5.2.3 Comparison between the QXRD and QSEM results

The benefit of using QXRD analysis is that the results obtained are primarily related to the GB particles while the QOM analysis includes the GB particles, the later formed  $\eta$  and  $\beta$  precipitates and other particles. In addition, QOM gives useful quantitative information on the quantities of the particles formed during homogenization. In Fig. 20, as discussed earlier, the increase in the volume fraction of particles during homogenization at low temperatures, is due to the formation of new precipitates ( $\eta$  and  $\beta$ ) rather than the increase in the GB particles. On the other hand, the volume fraction of the GB particles is almost unchanged, as shown in Fig. 22. Therefore, the combination of the results from QOM and QXRD quantitative analyses is essential to investigate the evolution of the microstructure during homogenization treatment.

The slight decrease in the fraction of the GB particles during homogenization at low temperatures means that the kinetics of the dissolution of these particles at low temperatures (< 430°C) is relatively slow. Since the fraction of the GB particles decreases significantly during homogenization at 510 °C and higher, it is concluded that in order to dissolve the GB particles, applying a homogenization treatment at 510 °C or higher is necessary.

In the case of QSEM analysis, an unchanged width means that no dissolution has occurred and any decrease in the width of the GB particles is the result of dissolution. The general trend of the change in the width of the GB particles during homogenization using QSEM analysis (Fig. 23) agrees with that of the fractions of the particles from QXRD analysis.

5.3 LMP phases

5.3.1 Results of quantitative analysis using FEG-SEM (QSEM)

Fig. 24 shows the radii of the particles obtained from FEG-SEM after homogenization at various conditions. For these experimental data, EDX analysis was first performed on the

particles which morphologically resembled the LMP phases. The radii of more than 10 particles in each homogenization condition, after ensuring that these were the LMP phases, were measured and the average is reported. The particle radius of zero in this figure indicates that no particles with the composition of the LMP phases were found in the structure, having the same methodology for the prediction of these particles with FEG-SEM at the same magnification. Therefore, the radius of the particles in this case was considered to be zero. It can be observed that the average radius of the LMP phase particles decreases gradually with time during homogenization at 430 and 470 °C.

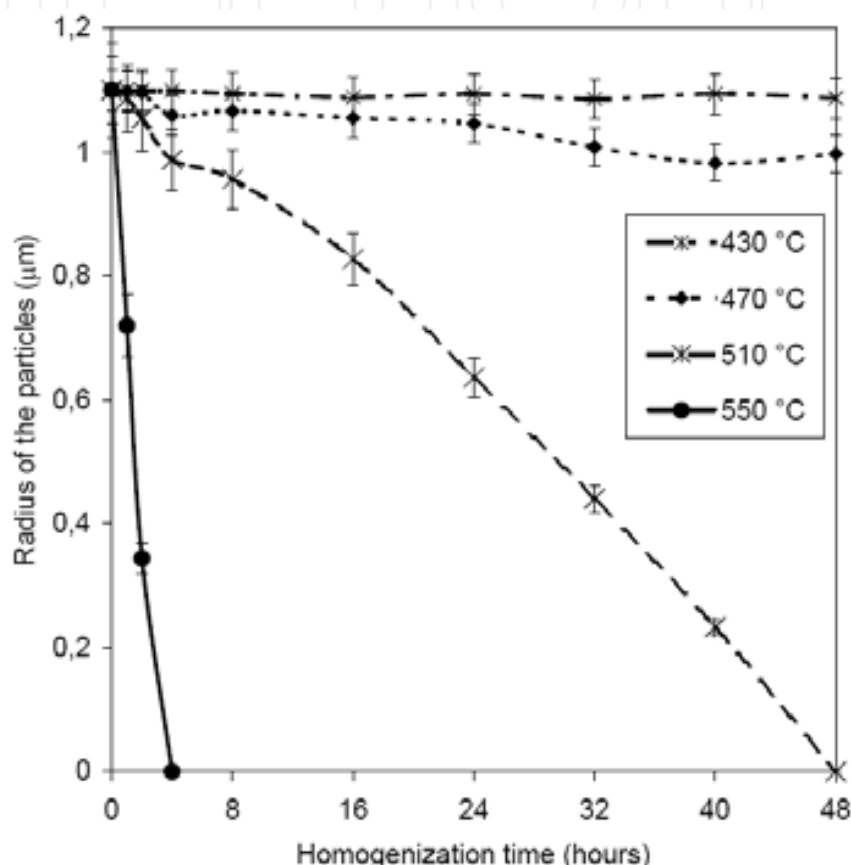


Fig. 24. Average radii of LMP phase at different homogenization conditions in the alloy variant N2 [53]

### 5.3.2 Results of quantitative differential scanning calorimetry (QDSC)

Fig. 25 shows that after homogenization at a moderate temperature, e.g., 470 °C, the LMP phases are still present in the structure, even after 48 h. At 510 °C, however, the LMP phases are fully dissolved within 48 h and at 550 °C within 2 h, as shown in Fig. 25. This is due to the large increases in the diffusion rates of the elements (i.e., Mg, Cu and Zn) at a high homogenization temperature. Therefore, it is necessary to employ a homogenization treatment at 510 °C for 48 h or 550 °C for 2 h to dissolve the LMP phases.

Fig. 26 gives a close-up view of the peaks in the DSC profiles of the samples homogenized at 470 °C for different hold times. It is clear that the peak intensity decreases with increasing homogenization time up to 48 h, which indicates the decreasing volume fraction of the LMP phases during homogenization at 470 °C.



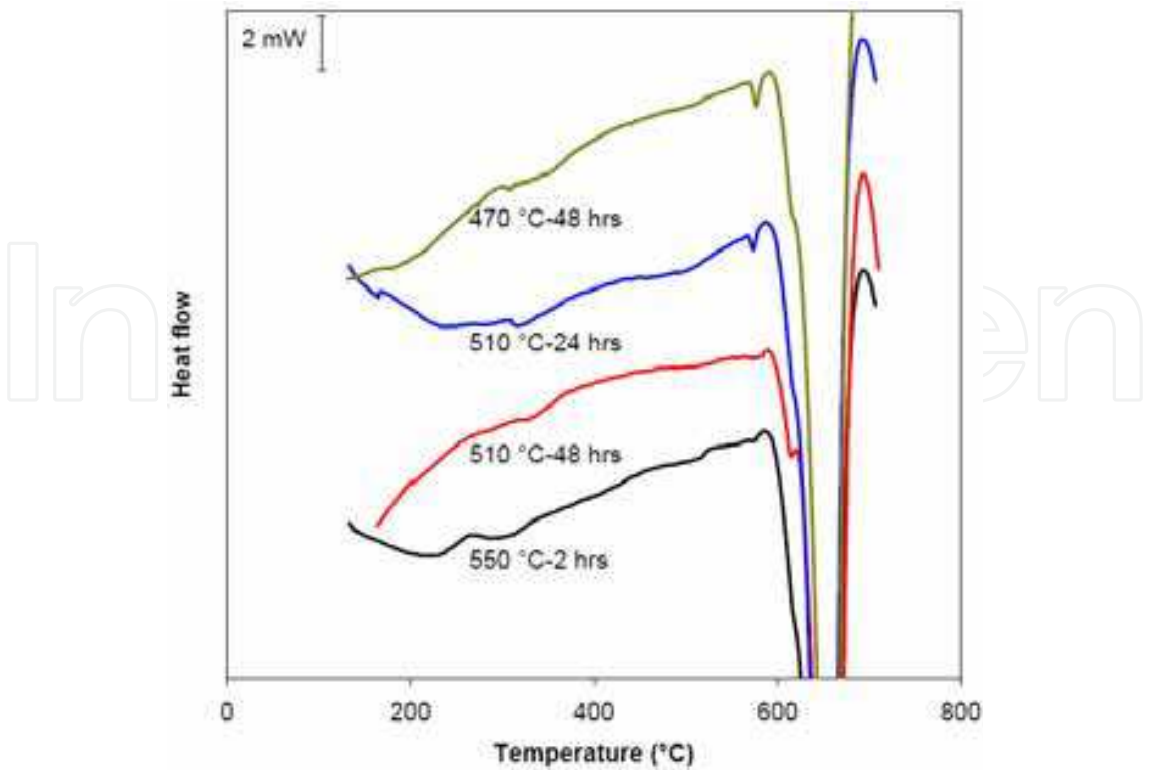


Fig. 25. DCS profiles of the samples homogenized at 470, 510 and 550 °C for different times [53]

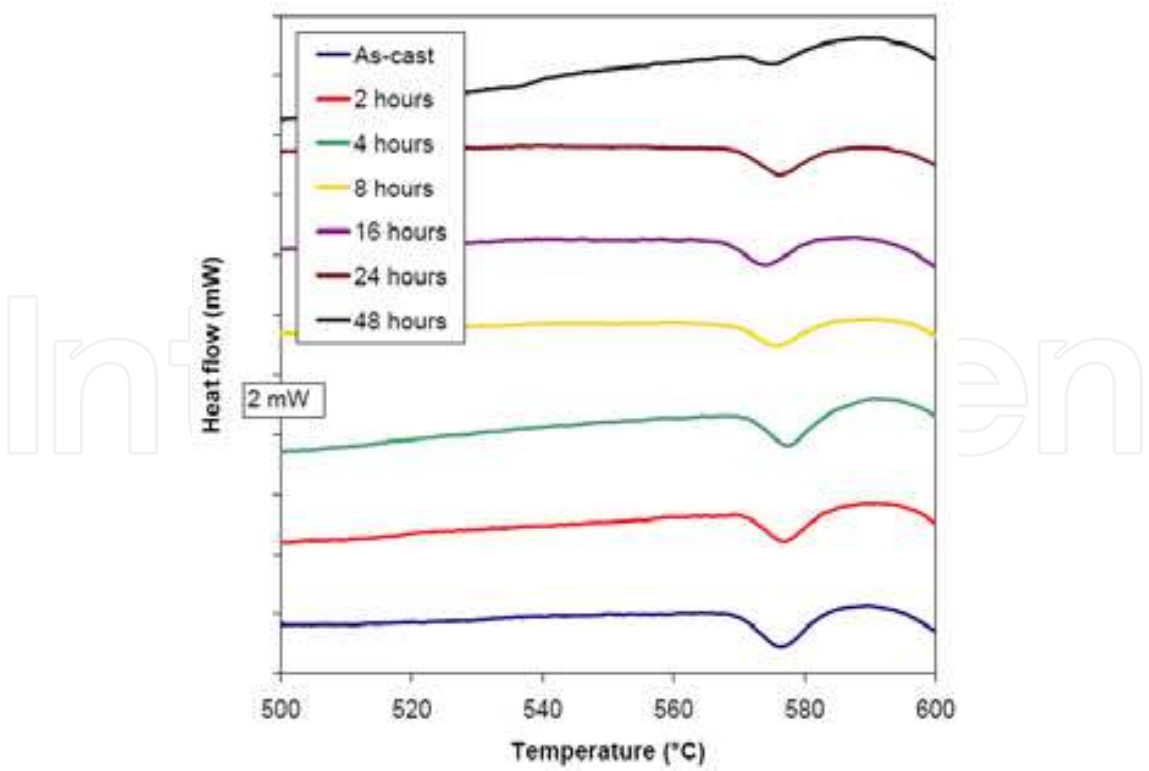


Fig. 26. Regions close to the peaks of the DSC profiles of the samples homogenized at 470 °C for different times (alloy variant N2) [53]

Fig. 27 shows the calculated volume fractions of the LMP phases at different homogenization conditions from the intensities of the DSC peaks, using Eqs. (4) and (5). It is clear that the volume fraction of the dissolved LMP phases increases with time during homogenization. Moreover, the volume fraction of the dissolved LMP phases is larger at a higher temperature and full dissolution only occurs at 510 or 550 °C at reasonable times (less than 48 h).

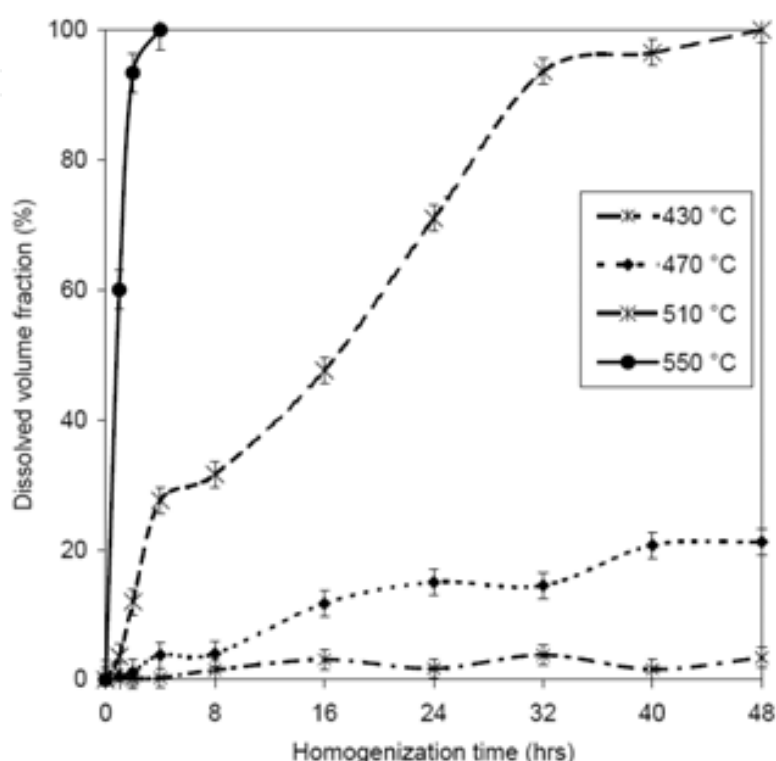


Fig. 27. Volume fractions of the dissolved LMP phases at different homogenization conditions (alloy variant N2) [53]

## 6. Formation of dispersoids

### 6.1 Detection of different dispersoid types

Table 8 shows the results of EDX analysis on more than 450 dispersed particles in a size range of less than 100 nm, with different shapes and at different locations with respect to the grains, i.e., grain interior and grain boundary regions in the alloy variant N3 (Table 2) homogenized under various conditions. It was possible to differentiate between 4 types of dispersoids, Zr- (Type 1), Cr- (Type 2), Mn-containing (Type 3) dispersoids and the ones containing a mixture of various elements (Type 4). The number fraction of each dispersoid type, out of 450 dispersoids counted, is also presented in Table 8. It can be seen that 62% of the dispersoids are Zr-containing ones, which indeed account for the majority of the dispersed particles. The number fractions of the other types (2, 3 and 4) are 23, 14 and 1%, respectively. Also shown in Table 8, at the grain boundary regions, i.e., 5  $\mu\text{m}$  from both sides of the grain boundary particles ( $\text{Al}_{17}(\text{Fe}_{3.2}\text{Mn}_{0.8})\text{Si}_2$  particles), the number fraction of the Mn-containing dispersoids (Type 3) reaches 93 %. However, this type of dispersoids was only observed after homogenization at 510 °C and higher, and especially for a holding time of 4 h or longer. It can be seen that the number fraction of Zr- and Cr-containing dispersoids at the grain boundary regions are only 2 and 1%, respectively.

Dispersoid type	Mg	Fe	Zn	Zr	Cr	Mn	Al	Number fraction (%) out of total 450 dispersoids analyzed	Number fraction (%) out of 75 dispersoids analyzed at the GB at T≥510°C, time≥4 hrs
Type 1 (Zr-containing)	0.08	0.67	0.1	11.9	0.3	0.09	86.86	62	2
Type 2 (Cr-containing)	0.23	11	0.82	0.6	34.1	0.0	53.22	23	1
Type 3 (Mn-containing)	0.09	7.3	0.26	0.2	0.02	12.8	79.33	14	93
Type 4	4.59	3.2	10.24	0.07	0.12	0.07	81.71	1	4

Table 8. Chemical compositions and number fractions of different types of dispersoids detected in the microstructure of the alloy variant N3

Fig. 28 (a) gives a close-up view of the different types of dispersoids. It is clear that the semi-spherical Zr-containing ones (Type 1) are the smallest, while the Cr-containing ones (Type 2) which are fully spherical are the largest. The small sizes of the Zr-containing dispersoids may be attributed to the very low diffusion rate of this element in the aluminum matrix and high nucleation rate [61]. Type 3, also semi-spherical in shape, is not present in the grain interior, thus not shown in Fig. 28 (a). It is presented in Fig. 29. Type 4 which has an elliptic or rod shape morphology is also shown in Fig. 28 (a). To assure the trustfulness of the particles determined with FEG-SEM, TEM analysis was also performed on the same sample and the results are presented in Fig. 28 (b). It can be seen that the same three different types of dispersoids are present in the TEM image with an approximately the same size range.

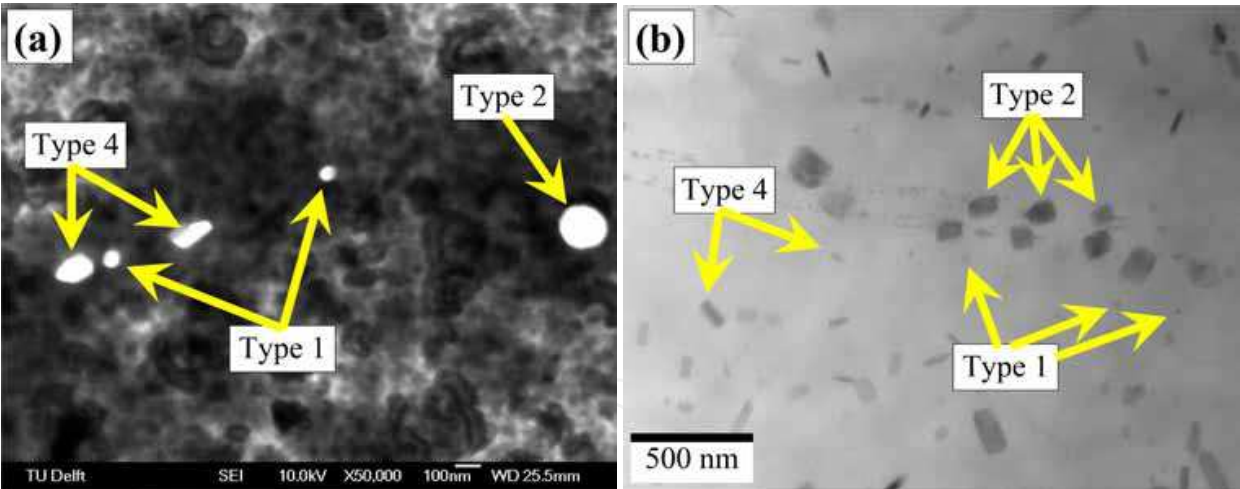


Fig. 28. (a) Close-up view of the different types of dispersoids in a sample homogenized at 510 °C for 8 h and (b) TEM image of the dispersoids in the same sample (alloy variant N3) [62]

Fig. 29 shows the distributions of the different types of dispersoids after homogenization. Fig. 29 (a) and (b) which illustrates the distributions of Zr- and Cr-containing dispersoids (Type 1 and 2) were captured in the grain interior. The number densities of these types decrease significantly with decreasing distance toward the grain boundaries. Fig. 29 (c) illustrates the distribution of Mn-containing dispersoids in the vicinity of an  $\text{Al}_{17}(\text{Fe}_{3.2}\text{Mn}_{0.8})\text{Si}_2$  particle. It is clear that most of the particles in this region are Mn-containing dispersoids. Their number density inside the grain interior is however almost

zero. During the analysis, it was not possible to capture a region with a sufficiently large number of Type 4 dispersoids. Therefore, no figure showing the distribution of this type can be presented in Fig. 29.

Quantitative Zr, Cr and Mn measurements from a line-scan across a grain in the as-cast microstructure of the AA7020 alloy are shown in Fig. 30. It can be seen that the concentrations of Zr and Cr in the grain interior are higher than what would be expected from the peritectic Al-Zr and Al-Cr phase diagrams [65, 66]. The lowest concentrations of Zr and Cr are found at the grain boundaries, which is in agreement with the finding of other researchers [15, 20, 25, 39]. The fluctuations in the Zr concentration across the analyzed region reflect the underlying dendritic structure within each grain. The measurements made close to the centre of the dendrite arms show that the Zr and Cr concentrations exceed their nominal values of 0.2 and 0.1 wt.% in the alloy variant N3, respectively. These regions solidified first during DC-casting and were thus enriched in Zr and Cr. However, a large fraction of grains contained Cr below its nominal value. In particular, low Cr levels were

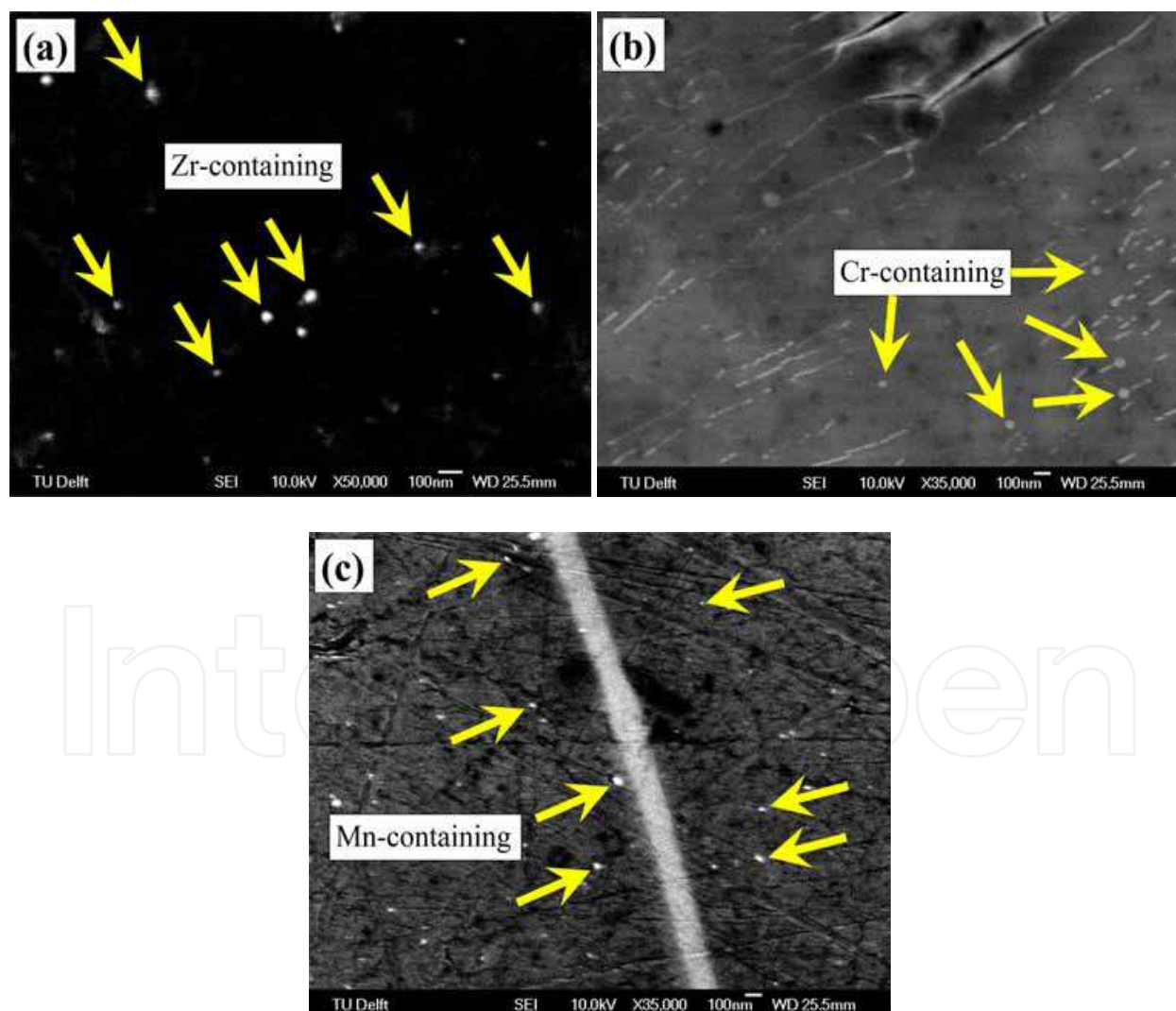


Fig. 29. Distributions of the different types of dispersoids after homogenization at 510 °C for 8 h, (a) Type 1 (Zr-containing), (b) Type 2 (Cr-containing) and (c) Type 3 (Mn-containing) (alloy variant N3) [62-64]



found near the grain boundaries and interdendritic regions. Therefore, it can be concluded that the reason for the small numbers of Cr-containing dispersoids in the grain boundary regions is the negligible concentrations of this element in these regions due to microsegregation during DC-casting. However, the fluctuations in the Zr level are not significant. The lowest Zr level is close to 0.13 wt.%.

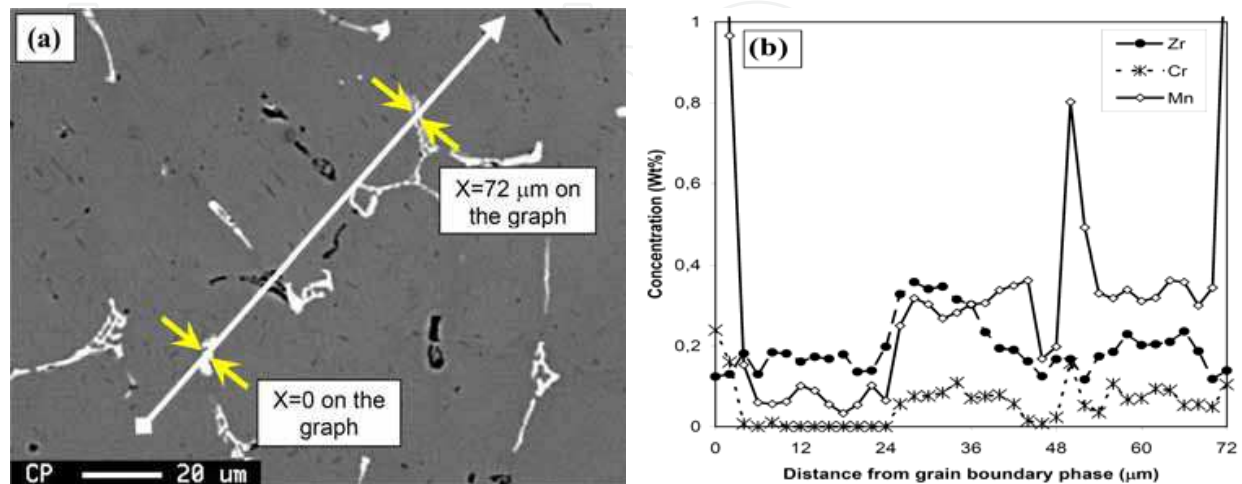


Fig. 30. (a) An EPMA scan and (b) analysis showing segregated Zr, Cr, Mn and Al at the cell boundaries of the as-cast microstructure in the AA7020 aluminum alloy variant N3 [62–64]

As indicated earlier, most of the dispersoids in the grain boundary regions are Mn-containing dispersoids. They are almost absent in the grain interior. The results of the EPMA analysis confirmed that the Mn concentration in the as-cast microstructure in the grain interior is less than the solid solubility limit of Mn at the mentioned homogenization temperatures [48]. Therefore, the reason for no Mn-containing dispersoids formed in the grain interior is a very small concentration of Mn in this region. The peak in the Mn concentration presented in Fig. 30, corresponds to the measurements made on or close to the intermetallic  $\text{Al}_{17}(\text{Fe}_{3.2}\text{Mn}_{0.8})\text{Si}_2$  particles (GB particles) at the grain boundaries. The small concentrations of Mn in the grain interior and the peaks in Fig. 30 indicate that, during solidification, most of the Mn element localized in the grain boundary regions formed the  $\text{Al}_{17}(\text{Fe}_{3.2}\text{Mn}_{0.8})\text{Si}_2$  particles located at the grain boundaries.

As mentioned earlier, the Mn-containing dispersoids form only at high temperatures ( $> 510^\circ\text{C}$ ) and holding times longer than 4 h and in the grain boundary regions. During homogenization at high temperatures,  $\text{Al}_{17}(\text{Fe}_{3.2}\text{Mn}_{0.8})\text{Si}_2$  particles may dissolve in the microstructure, thus increasing the Mn concentration in the grain boundary regions. Fig. 31 shows the EPMA measurements of the Mn concentration from a line scan across a grain in a sample homogenized at  $550^\circ\text{C}$  for 8 h. It is clear that the Mn concentration in the regions close to the  $\text{Al}_{17}(\text{Fe}_{3.2}\text{Mn}_{0.8})\text{Si}_2$  particles increases, which is attributed to the dissolution of  $\text{Al}_{17}(\text{Fe}_{3.2}\text{Mn}_{0.8})\text{Si}_2$  particles during homogenization under this condition. This results in the formation of Mn-containing dispersoids close to the grain boundaries. However, the Mn concentration in the grain interior only changes slightly as confirmed by the present EPMA analysis (Fig. 31), mainly because of the low diffusion rate of Mn in the aluminum matrix [67]. As a result, the Mn concentration is too small in the grain interior to form the Mn-containing dispersoids.

From Fig. 29, it is clear that the Cr-containing dispersoids (Type 2) have a localized distribution in the grain interior. The localized distribution of the Cr-containing dispersoids together with the fact that they are larger than the other types of particles may indicate that this type of dispersoids form heterogeneously, which is in agreement with other investigations [34]. The heterogeneous nucleation of the Cr-containing dispersoids on the u-phases in the case of Al-Mg-Si alloys has been documented [34]. It was observed that during the heating of the as-cast Al-Mg-Si alloys to 580 °C an intermediate phase, referred to as the 'u-phase' nucleated on the  $Mg_2Si$  needles. The phase was rich in Mn or Cr. Upon continued heating, the dispersoids containing Mn and Cr nucleated heterogeneously on the 'u-phase' precipitates before these precipitates were dissolved.

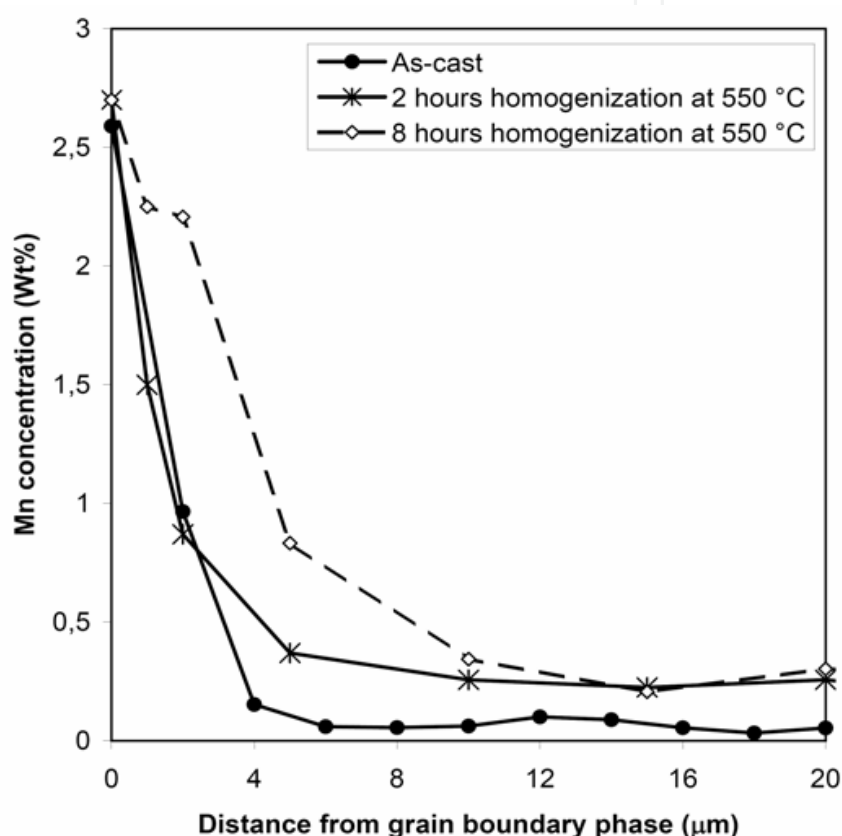


Fig. 31. EPMA scan analysis showing the Mn concentration across a grain of the AA7020 aluminum alloy (alloy variant N3) homogenized at 510 °C for 8 h [62, 64]

To make a solid conclusion on various dispersoids formed during homogenization, they were characterized with respect to formation temperature, size, location and morphology. Table 9 shows the characteristics of the four types of dispersoids formed in the homogenized AA7020 alloy. The deviation expresses the ratio of the number of the particles (with the mentioned characteristics) that showed different chemical compositions to the total number of the particles (with the mentioned characteristic) that were analyzed. The Zr-, Cr- and Mn-containing dispersoids have deviations of only 3, 5 and 4.5 %, respectively. It indicates that the characteristics presented in Table 9 are reasonably accurate to differentiate between these types of dispersoids. It should be noted that the deviation of Type 4 is not reported since the dispersed particles of this type are rare in the microstructure.

Dispersoid type	Major elements	Formation temperature (°C)	Location	Radius (nm)	Morphology	Distribution	Deviation (%) *
Type 1	Zr	390 – 550	Center of the grains	<25	Semi-spherical	Uniform	3
Type 2	Cr, Fe	390 – 550	Center of the grains	25-100	Fully spherical	Localized	5
Type 3	Mn, Fe	T ≥ 510 °C	Close to the GB phases	<50	Semi-spherical	Uniform	4.5
Type 4	Mg, Zn, Fe	390 – 550	All	25-100	Elliptic	Uniform	---

\* The deviation expresses the ratio of the number of the particles with the mentioned characteristics that showed different chemical compositions to the total number of analysed particles with the same characteristics.

Table 9. Characteristics of different types of dispersoids in AA7020 after 4 h homogenization at different temperatures

6.2 Evolution of Zr-containing dispersoids during homogenization

As mentioned in Table 8, Zr-containing dispersoids constitute about 62 % of all dispersoids present in the microstructure of the alloy (N3) after homogenization. Therefore, they can be considered the most important ones for recrystallization inhibition. In addition, due to their higher number density, it is easier to quantify them and their evolution during homogenization. Fig. 32 presents typical FEG-SEM images of the Zr-containing dispersoids and related size distribution graphs in the central region of a grain. The size distribution graphs were obtained using the Johnson-Saltykov method as mentioned in the experimental procedure [48] and therefore, the x axis has logarithmic size distribution categories, which is finer at lower values and vice versa.

It should be mentioned that in order to evaluate the efficiency of a homogenization treatment on the inhibition of recrystallization, all relevant parameters including size, size distribution and volume fraction of particles should be taken into consideration, which have been incorporated into an equation of Zener drag pressure [30]. This equation has recently been developed to include the effect of size distribution of dispersoids [3, 68]. The intention of preparing this chapter is to investigate the microstructural evolution during homogenization and therefore, discussion on the effect of homogenization treatment on recrystallization inhibition has been avoided. For more details, the reader is referred to other references [3, 63, 64, 68, 69].

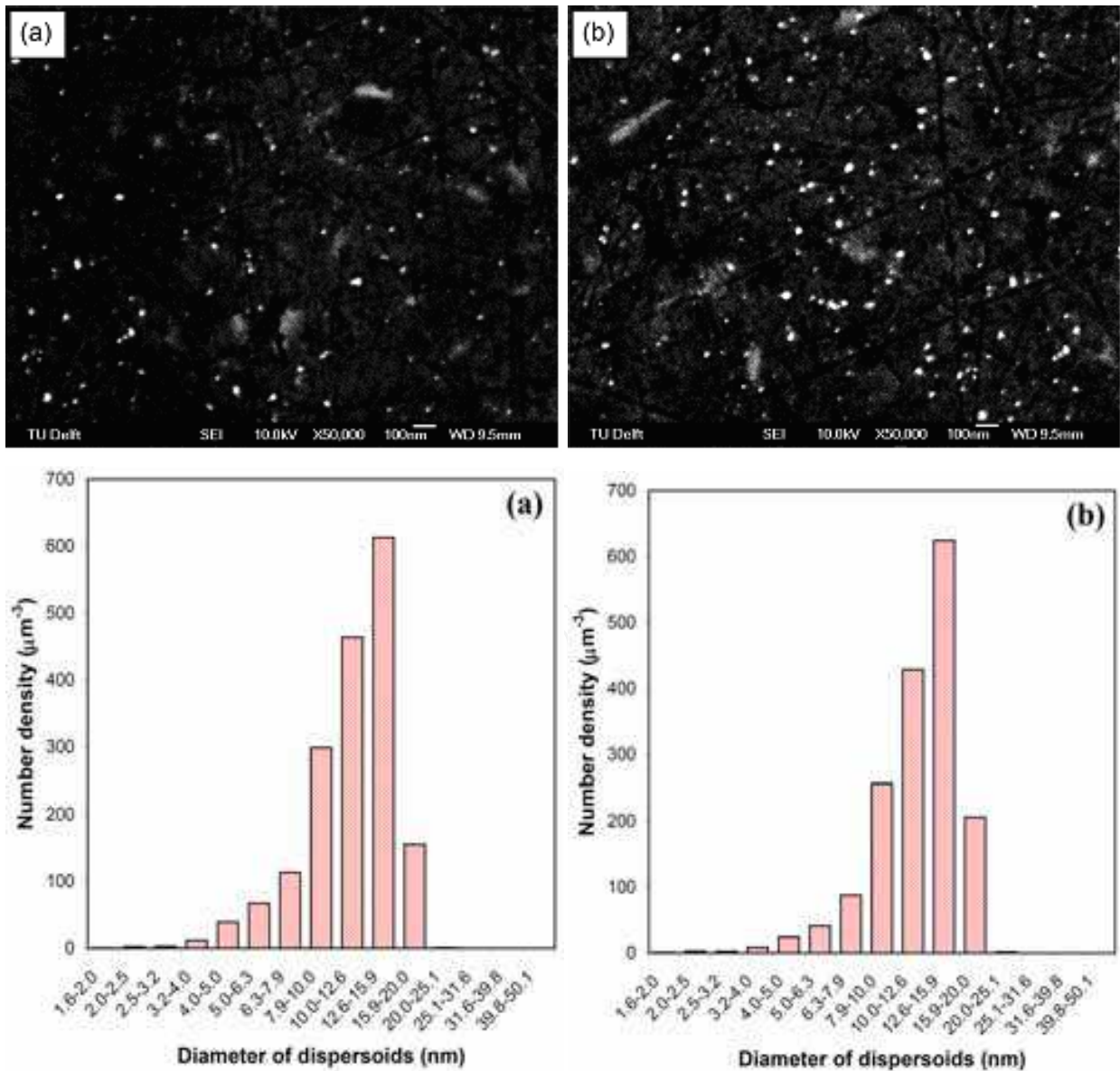
The number density of the Zr-containing dispersoids decreases significantly with increasing distance towards the grain boundaries. This can be attributed to the segregation of zirconium during solidification. It is clear that the sizes and number densities of the Zr-containing dispersoids change with homogenization condition.

Comparison between Figs. 32 (a) and (b) shows that at a given temperature, the sizes increase slightly with time while the number densities remain almost unchanged. In addition, the number of particles of larger sizes, i.e., larger than 15-20 nm, increased with increasing homogenization time at a certain temperature. Comparison between Figs. 32 (b) and (c) for a given composition of the alloy variant N3 and different homogenization temperatures demonstrates that at a higher homogenization temperature e.g., 550 °C, Fig. 32 (c), a larger fraction of particles are of large sizes and the number densities are relatively small, which may be considered as a sign of coarsening. In addition, paying attention to the effect of chemical composition in Fig. 32 (b) (for alloy variant N3) and Fig. 32 (d) (for alloy variant N1), one can find reasonably similar size distributions with different number

densities. The sizes are almost constant while the number densities increase significantly with increasing Zr content in the alloy.

Fig. 33 (a) shows the effect of homogenization time on the diameters of the Zr-containing dispersoids at different homogenization temperatures. It is clear that at each homogenization temperature, the average dispersoid diameter increases with increasing holding time and then tends to reach a constant value. In addition, the average diameter is also a function of homogenization temperature. At a higher temperature, the dispersoid diameter is larger.

The effect of homogenization time on the number density of the dispersoids at different homogenization temperatures is illustrated in Fig. 33 (b). It can be seen that with increasing holding time, the number density increases and then stays at a certain level. In addition, the number density of the dispersoids formed at 470 °C is significantly larger than that formed at 390 or 550 °C, while the difference between 390 and 550 °C in the dispersoid number density is considerably smaller.





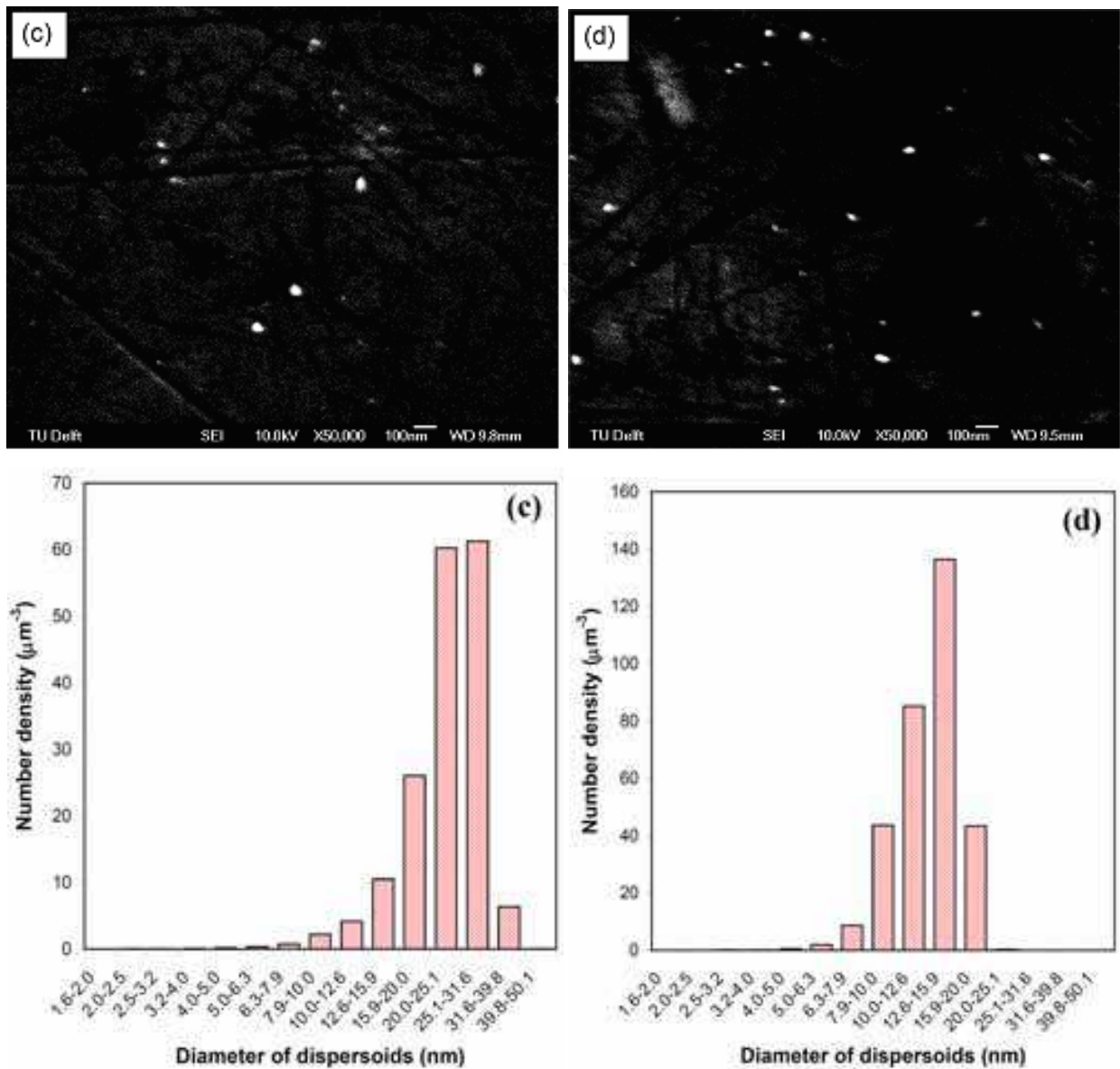


Fig. 32. Typical SEM micrographs showing the effects of homogenization parameters and Zr content on the sizes and size distributions of the Zr-containing dispersoids (a) alloy variant N3, T=470 °C for 8 h, (b) N3, T= 470 °C for 24 h, (c) alloy variant N3, T=550 °C for 24 h and (d) alloy variant N1, T= 470 °C for 24 h [63, 69]

Fig. 34 (a) shows the effect of Zr content on the average diameter of dispersoids formed at 470 °C as a function of time. It can be seen that the average diameter of the dispersoids formed in the alloy with the highest Zr content are larger than those in the other two alloys. However, this effect is not very strong, as the average dispersoid diameters in the N1 and N2 variants do not differ much from each other. An increase in the average diameter of the dispersoid particles with increasing homogenization time towards a constant value is also observed for the alloy variants with different Zr contents. Fig. 34 (b) presents the effect of Zr content on the number density of the Zr-containing dispersoids homogenized at 470 °C. It is clear that the Zr-content has a strong effect on the number density of the dispersoids. The number density of the dispersoids for the alloy with a Zr content of 0.2 wt.% is almost two times as much as that in the alloy with a Zr-content of 0.13 wt.%.

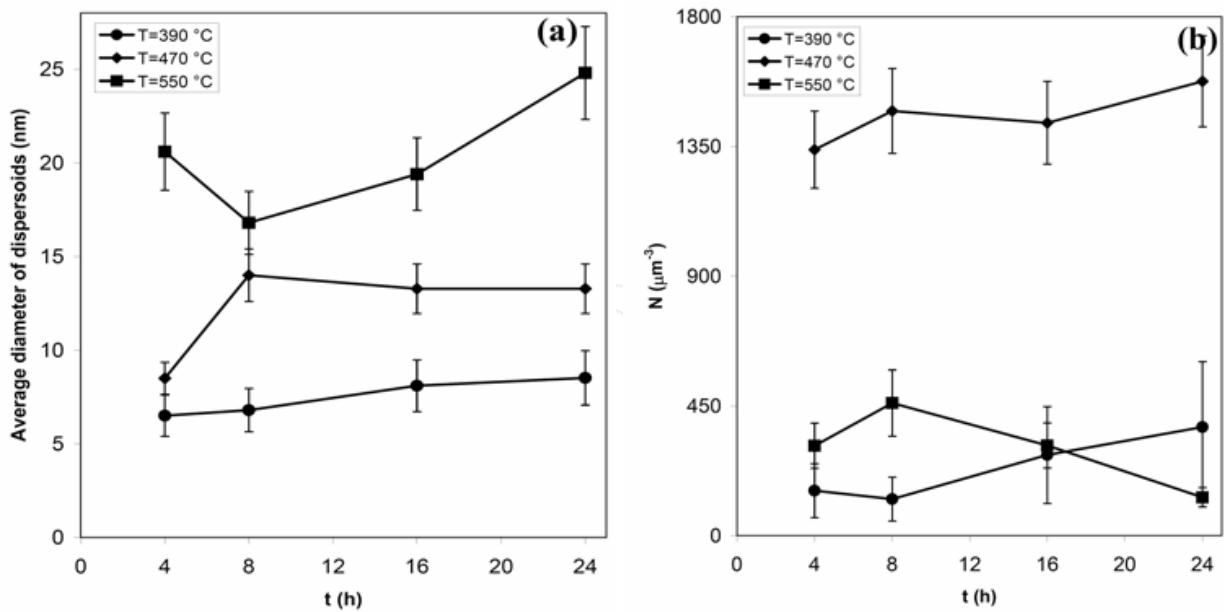


Fig. 33. Effect of homogenization time on the (a) average diameter and (b) number density of the Zr-containing dispersoids in the alloy variant N2 homogenized at different temperatures [62, 69]

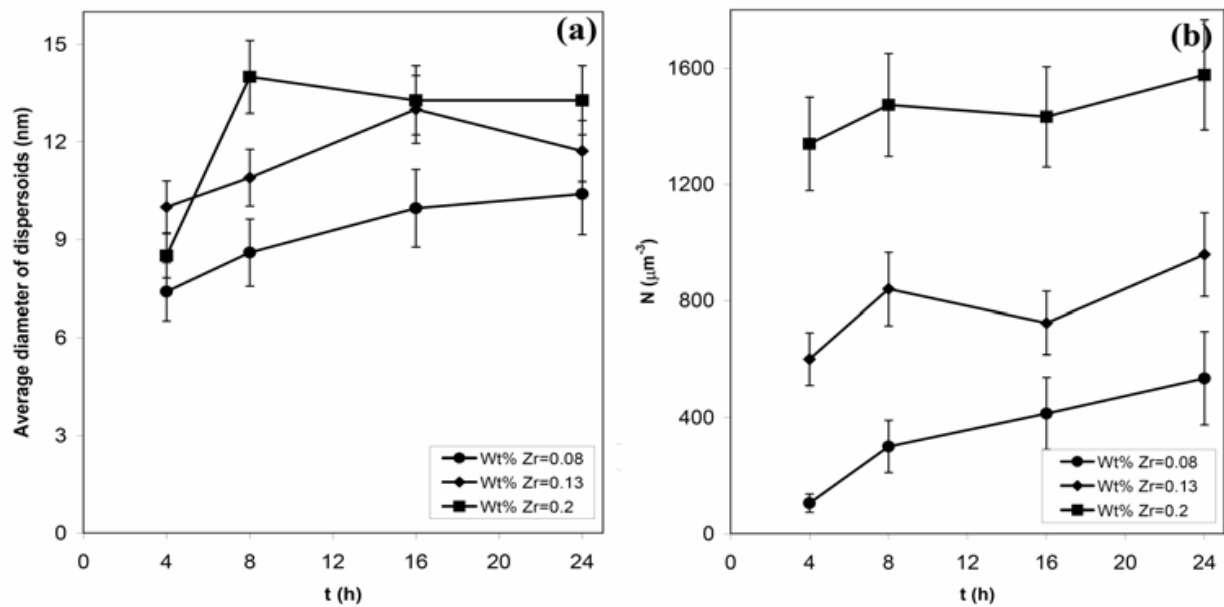


Fig. 34. Effect of Zr content on the (a) average diameter and (b) number density of dispersoids formed at 470 °C as a function of homogenization time [62, 69]

7. Conclusions

Main particles detected in the as-cast microstructure of AA7020 aluminum alloys were categorized to be grain boundary ones, low melting point particles and dispersoids. The evolution of these particles during the homogenization treatment of the AA7020 aluminum alloy was quantitatively analyzed and the following conclusions have been drawn.

- 1) The particles distributed along the grain boundaries which constitute more than 70% of the secondary phases present in the as-cast structure of the AA7020 aluminum alloy are  $\text{Al}_{17}(\text{Fe}_{3.2}\text{Mn}_{0.8})\text{Si}_2$  particles. The low melting point phases are indeed present in the as-cast microstructure of the AA7020 aluminum alloy, which may cause incipient melting at 576 °C. These phases contain Al-Cu-Mg-Zn and dissolve during homogenization at 550 °C for 2 h.
- 2) The width of the grain boundary particles remains unchanged during homogenization at low temperatures. It however decreases at higher temperatures. The extent of the dissolution is more dependent on homogenization temperature than on time. The evolution mechanisms of the GB particles during homogenization consist of spheroidization during homogenization at low temperatures and thinning, discontinuation and full dissolution (TDFD) at high temperatures.
- 3) Four different types of dispersoids are formed in the AA7020 aluminum alloy variants during homogenization. In addition to the well-known  $\text{Al}_3\text{Zr}$  dispersoids, three other types of dispersoids are also present in the homogenized microstructure of the AA7020 aluminum alloy. The number densities of Zr- and Cr-containing dispersoids are large in the grain interior and very small in the grain boundary regions. These two types of dispersoids appear to be fully spherical and are formed at all the homogenization conditions. The Mn-containing dispersoids form only when the homogenization temperature is equal to or higher than 510 °C and holding time longer than 4 h. The number density of these dispersoids is close to zero in the grain interior but becomes high in the grain boundary regions. The number density and sizes of the Zr-containing dispersoids increase with increasing Zr content of the alloy and homogenization time.

## 8. Acknowledgments

This research was carried out under the project number MC 4.04203 in the framework of the Research Program of the Materials innovation institute M2i ([www.m2i.nl](http://www.m2i.nl)). The authors acknowledge Mr. K. Kwakernaak and Mr. E.R. Peekstok for assistance in microstructure examination.

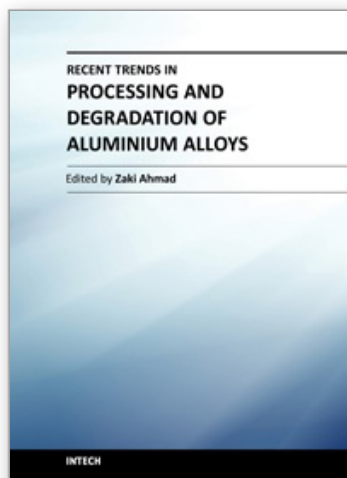
## 9. References

- [1] ASM Handbook, 10th ed., vol. 14, Metal Forming, ASM International, Metals Park, OH (1992).
- [2] T. Sheppard, *Extrusion of Aluminum Alloys*, Kluwer Academic Publishers, Dordrecht (1999).
- [3] A.R. Eivani, Modeling of Microstructural Evolution during Homogenization and Simulation of Transient State Recrystallization leading to Peripheral Coarse Grain Structure in Extruded Al-4.5Zn-1Mg Alloy, PhD Thesis, June 2010, Delft, The Netherlands.
- [4] N.A. Belov, D.G. Eskin and A.A. Aksenov, *Multicomponent Phase Diagrams: Applications for Commercial Aluminum Alloys*, Elsevier Science, New York (2005).
- [5] L.L. Rokhlin, T.V. Dobatkina, N.R. Bochvar and E.V. Lysova, *J Alloys Compd.* 367, 10 (2004).
- [6] S.T. Lim, Y.Y. Lee and I.S. Eun, *Mater. Sci. Forum* 519-521, 549 (2006).
- [7] C. Mondal and A.K. Mukhopadhyay, *Mater. Sci. Eng. A* 391, 367 (2005).
- [8] R.K. Gupta, N. Nayan and B.R. Ghosh, *Can. Metall. Q.* 45, 347 (2006).

- [9] H. Ahmed, A.R. Eivani, J. Zhou and J. Duszczuk, Proc. Symp. *Aluminum Alloys: Fabrication, Characterization and Application*, TMS Annual Meeting, New Orleans (2008).
- [10] N. Parson, and C. Jowett, Proc. 3rd Australasian Pacific Aluminium Extrusion Conference, Sydney, Australia, (2005).
- [11] N. Parson, S. Barker, A. Shalanski and C. Jowett, Proc. 8th Int. Aluminum Extrusion Technology Seminar, vol. 1 (2004).
- [12] A.R. Eivani, H. Ahmed, J. Zhou and J. Duszczuk, Proc. Symp. *Aluminum Alloys: Fabrication, Characterization and Application*, TMS Annual Meeting, New Orleans (2008).
- [13] J.W. Martin, *Precipitation Hardening*, 2nd ed., Butterworth-Heinemann, Oxford (1998).
- [14] A. Jackson and T. Sheppard, Proc. 6th Int. Aluminum Extrusion Technology Conf., Chicago, Aluminum association, Washington DC, vol. 1 (1996).
- [15] J.D. Robson and P.B. Prangnell, *Acta Mater.*, 49, 599 (2001).
- [16] G.T. Hahn and A.R. Rosenfield, *Metall. Trans. A*, 6, 653 (1975).
- [17] D.S. Thompson, *Metall. Trans. A*, 6, 671 (1975).
- [18] G.G. Garrett and J.F. Knott, *Metall. Trans. A*, 9, 1187 (1978).
- [19] F.Y. Xie, T. Kraft, Y. Zuo, C.H. Moon and Y.A. Chang, *Acta Mater.*, 47, 489 (1999).
- [20] B. Morere, C. Maurice and R. Shahani, J. Driver, *Metall. Mater. Trans. A* 32, 625 (2001).
- [21] E. Clouet, A. Barbu, L. Lae and G. Martin, *Acta Mater.* 53, 2313 (2005).
- [22] Z. Jia, G. Hua, B. Forbord and J.K. Solberg, *Mater. Sci. Eng. A* 444, 284 (2007).
- [23] B.L. Ou, J.G. Yang and M.Y. Wei, *Metall. Mater. Trans. A* 38, 1760 (2007).
- [24] J.D. Robson, M.J. Jones and P.B. Prangnell, *Acta Mater.* 51, 1453 (2003).
- [25] J.D. Robson, *Acta Mater.* 52, 1409 (2004).
- [26] J.D. Robson, *Acta Mater.* 52, 4669 (2004).
- [27] O.N. Senkov, R.B. Bhat, S.V. Senkova and J. Tatalovich, *Mater. Forum* 28 (2004).
- [28] X. Fan, D. Jiang, Q. Meng and L. Zhong, *Mater. Lett.* 60, 1475 (2006).
- [29] R. Ciach and B. Dukiet-Zawadzka, *J Mater. Sci.* 13, 2676 (1978).
- [30] F.J. Humphreys and M. Hatherly, *Recrystallization and Related Annealing Phenomena*, 3rd ed., Elsevier Science Inc., Oxford (1995).
- [31] M. Peters, J. Eschweiler and K. Welpmann, *Scripta Metall.* 20, 259 (1986).
- [32] O. Daaland and E. Nes, *Acta Mater.* 44, 1413 (1996).
- [33] Y.J. Li and L. Arnberg, *Acta Mater.* 51, 3415 (2003).
- [34] L. Lodgaard and N. Ryum, *Mater. Sci. Eng. A* 283, 144 (2000).
- [35] M. Cabibbo, E. Evangelista, C. Scalabroni and E. Bonetti, *Mater. Sci. Forum* 503-504, 841 (2006).
- [36] L. Lodgaard and N. Ryum, *Mater. Sci. Tech.* 16, 599 (2000).
- [37] D.H. Lee, J.H. Park and S.W. Nam, *Mater. Sci. Tech.* 15, 450 (1999).
- [38] R.A. Jeniski, B. Thanaboonsombut and T.H. Sanders, *Metal. Mater. Trans. A* 27, 19 (1996).
- [39] J.D. Robson, *Mater. Sci. Eng. A* 338, 219 (2002).
- [40] S.V. Senkova, O.N. Senkov and D.B. Miracle, *Metal. Mater. Trans. A* 37, 3569 (2006).
- [41] O.N. Senkov, R.B. Bhat, S.V. Senkova and J.D. Schloz, *Metal. Mater. Trans. A* 36, 2115 (2005).
- [42] A. Deschamps and Y. Bréchet, *Mater. Sci. Eng. A* 251, 200 (1998).
- [43] J.T. Armstrong, in K.F.J. Heinrich, D.E. Newbury (Eds), *Electron Probe Quantitation*, Plenum Press, New York (1991).
- [44] B.D. Cullity, S.R. Stock and S. Stock, *Elements of X-Ray Diffraction*, 3rd ed., Prentice Hall, New Jersey (2001).



- [45] Alphabetical indexes for experimental patterns, Sets 1-52, International Center for Diffraction Data (ICDD), 2005, Powder Diffraction File Number (PDF no.) 01-071-4015.
- [46] M. Cooper, *Acta Crystallogr.* 23, 1106 (1967).
- [47] ASM Handbook, 10th ed., vol. 2, *Non-Ferrous Alloys*, ASM International, Metals Park, OH (1992).
- [48] R.T. DeHoff and F.N. Rhines, *Quantitative Microscopy*, McGraw-Hill, New York (1968).
- [49] A.R. Eivani, H. Ahmed, J. Zhou, J. Duszczyk, *Metal. Mater. Trans. A.* 40, 717 (2009).
- [50] R.W. Cahn and P. Haasen, *Physical Metallurgy*, North Holland, Amsterdam (1996).
- [51] D. Gaskell, *Introduction to the Thermodynamics of Materials*, Taylor & Francis Co., New York (2003).
- [52] R. Nadella, D.G. Eskin, Q. Du and L. Katgerman, *Prog. Mater. Sci.* 53, 421 (2008).
- [53] A.R. Eivani, H. Ahmed, J. Zhou, J. Duszczyk, *Mater. Sci. Tech.* 26, 215 (2010).
- [54] M. Dumont, W. Lefebvre, B. Doisneau-Cottignies and A. Deschamps, *Acta Mater.* 53, 2881 (2005).
- [55] G. Sha and A. Cerezo, *Acta Mater.* 52, 4503 (2004).
- [56] A. Melander and P.A. Persson, *Acta Metall.* 26, 267 (1978).
- [57] ASM Handbook, 10th ed., vol. 3, *Alloy Phase Diagrams*, ASM International, Metals Park, OH (1992).
- [58] M. Conserva, E. Di Russo and A. Giarda, *J Metall.* 6, 367 (1973).
- [59] E. Ho and G.C. Weatherly, *Acta Metall.* 23, 1451 (1975).
- [60] A.R. Eivani, H. Ahmed, J. Zhou, J. Duszczyk, *Phil. Mag.* 42, 1109 (2010).
- [61] M. S. Zedalis and M. E. Fine, *Metall. Trans. A.* 17, 2187 (1986).
- [62] A.R. Eivani, H. Ahmed, J. Zhou, J. Duszczyk, C. Kwakernaak, *Mater. Sci. Tech.* DOI 10.1179/026708310X12635619988267 (2010).
- [63] A.R. Eivani, H. Ahmed, J. Zhou, J. Duszczyk, *Mater. Sci. Eng. A.* 527, 2418 (2010).
- [64] A.R. Eivani, S. Valipour, H. Ahmed, J. Zhou, J. Duszczyk, *Metal. Mater. Trans. A.* 40, 2435 (2009).
- [65] J. Murray, A. Peruzzi and J.P. Abriata, *J Phase Equilib.* 13, 227 (1992).
- [66] N. Saunders, *Z. Metallkd* 80, 894 (1989).
- [67] Y. Du, Y.A. Chang, B. Huang, W. Gong, J. Jin, H. Xu, Z. Yuan, Y. Liu, Y. He and F.Y. Xie, *Mater. Sci. Eng. A* 363, 140 (2003).
- [68] A.R. Eivani, S. Valipour, H. Ahmed, J. Zhou, J. Duszczyk, *Metal. Mater. Trans. A.* 42, 1109 (2011).
- [69] A.R. Eivani, H. Ahmed, J. Zhou, J. Duszczyk, *Adv. Mater. Res.* 89-91, 177 (2010).



### **Recent Trends in Processing and Degradation of Aluminium Alloys**

Edited by Prof. Zaki Ahmad

ISBN 978-953-307-734-5

Hard cover, 516 pages

**Publisher** InTech

**Published online** 21, November, 2011

**Published in print edition** November, 2011

In the recent decade a quantum leap has been made in production of aluminum alloys and new techniques of casting, forming, welding and surface modification have been evolved to improve the structural integrity of aluminum alloys. This book covers the essential need for the industrial and academic communities for update information. It would also be useful for entrepreneurs technocrats and all those interested in the production and the application of aluminum alloys and strategic structures. It would also help the instructors at senior and graduate level to support their text.

#### **How to reference**

In order to correctly reference this scholarly work, feel free to copy and paste the following:

Ali Reza Eivani, Jie Zhou and Jurek Duszczek (2011). Microstructural Evolution During the Homogenization of Al-Zn-Mg Aluminum Alloys, Recent Trends in Processing and Degradation of Aluminium Alloys, Prof. Zaki Ahmad (Ed.), ISBN: 978-953-307-734-5, InTech, Available from: <http://www.intechopen.com/books/recent-trends-in-processing-and-degradation-of-aluminium-alloys/microstructural-evolution-during-the-homogenization-of-al-zn-mg-aluminum-alloys>

**INTECH**  
open science | open minds

#### **InTech Europe**

University Campus STeP Ri  
Slavka Krautzeka 83/A  
51000 Rijeka, Croatia  
Phone: +385 (51) 770 447  
Fax: +385 (51) 686 166  
[www.intechopen.com](http://www.intechopen.com)

#### **InTech China**

Unit 405, Office Block, Hotel Equatorial Shanghai  
No.65, Yan An Road (West), Shanghai, 200040, China  
中国上海市延安西路65号上海国际贵都大饭店办公楼405单元  
Phone: +86-21-62489820  
Fax: +86-21-62489821

© 2011 The Author(s). Licensee IntechOpen. This is an open access article distributed under the terms of the [Creative Commons Attribution 3.0 License](https://creativecommons.org/licenses/by/3.0/), which permits unrestricted use, distribution, and reproduction in any medium, provided the original work is properly cited.

IntechOpen

IntechOpen